HOKKAIDO UNIVERSITY

Title	3D Tomography of Ionospheric Anomalies immediately before and after Large Earthquakes
Author(s)	Muafiry, Ihsan Naufal
Degree Grantor	北海道大学
Degree Name	博士(理学)
Dissertation Number	甲第14645号
Issue Date	2021-09-24
DOI	https://doi.org/10.14943/doctoral.k14645
Doc URL	https://hdl.handle.net/2115/83579
Type	doctoral thesis
File Information	Ihsan_Naufal_Muafiry.pdf



Hokkaido University Collection of Scholarly and Academic Papers : HUSCAP

3D Tomography of Ionospheric Anomalies immediately before and after Large Earthquakes

(巨大地震直前直後の電離圏異常の三次元トモグラフィー)



By

Ihsan Naufal Muafiry

Supervisor: Prof. Kosuke Heki

A dissertation submitted in partial fulfillment

of the requirements for the degree of

Doctor of Philosophy

Department of Natural History Science

Graduate School of Science, Hokkaido University

September 2021

Table of contents

Abstract 5

Acknowledgments 7

Chapter 1: Introduction 9

1.1 GNSS for Positioning 9

1.2 GNSS for Ionospheric Studies 10

1.3 Ionospheric Structure 12

1.4 Solid Earth and Ionosphere 14

1.5 Ionospheric Disturbance due to the Sea Surface Motion 16

1.6 Earthquake Precursors in Ionosphere 18

1.7 3D Tomography for Ionospheric Electron Density Anomalies 19

1.8 Research Objectives 20

Chapter 2: Data and Method 21

2.1 GNSS Network in Japan 21

2.2 GNSS Network in South Korea 22

2.3 GNSS Networks in South America 24

2.4 GNSS-TEC Method 25

2.5 Strategies to Isolate Anomalies from GNSS-TEC Data 28

2.6 Ionospheric 3D Tomography Method 29

Chapter 3: 3D Tomography of the Ionospheric Anomalies immediately before Earthquakes: The 2011 Tohoku-oki Earthquake 35

3.1 Introduction: History of Debate 36

3.2 Data set 39

3.3 Data Processing Strategy 40

3.3 Resolution tests 49

3.4 Tomography results 53

3.5 Growth and polarity balances of the preseismic anomalies 62

3.6 Discussion on the physical mechanism of the preseismic anomalies 63

Chapter 4: 3D Tomography of the Ionospheric Anomalies Before the 2010 Maule Earthquake, Chile: Comparison with the 2011 Tohoku-oki and 2015 Illapel Earthquake 68

4.1 Introduction: Structure of preseismic ionospheric anomalies 69

4.2 Data set 70

4.3 Data processing strategy 72

4.4 Resolution test 73

4.5 Tomography result 76

4.6 Comparison with the 2011 Tohoku-oki and 2015 Illapel Earthquakes 83

Chapter 5: 3D Tomography of the Ionospheric Anomalies after Earthquakes: The 2011 Tohoku-oki Earthquake 86

5.1 Introduction: Tsunamigenic ionospheric anomalies 87

5.2 Data set..... 87

5.3 Data processing strategy 87

5.4 Resolution tests 89

5.5 Tomography result 91

5.6 Physical mechanism of post-seismic anomalies 91

5.7 Origin of variety of waveforms..... 92

Chapter 6: Conclusions and Recommendation 94

6.1 Conclusions..... 94

6.2 Recommendation 97

Abstract

A dense network of ground global navigation satellite system (GNSS) receivers detected ionospheric total electron content (TEC) changes starting ~40 minutes before the 2011 Tohoku-oki (M_w 9.0) earthquake around the ruptured fault, together with the long-lasting postseismic TEC drop. In this study, I robustly estimate three-dimensional (3D) distribution of both pre- and post-seismic ionospheric anomalies of the 2011 M_w 9.0 Tohoku-oki and the 2010 M_w 8.8 Maule earthquakes by tomographic inversions of electron density anomalies. For the 2011 case, I set up more than 6,000 blocks, as large as 1.0^o (east-west) x 0.9^o (north-south) x 60 km (vertical), over the Japanese Islands, the Sea of Japan, and the Korean Peninsula, up to 870 km altitude. I used slant-TEC residuals obtained using 8 satellites and 1,493 ground stations as inputs to the 3D tomographic inversion. For the Maule earthquake, TEC data are obtained from 6 GNSS satellites and 89 ground stations mainly in Chile and Argentine. I set up >3,500 blocks, with the size of 1.0^o (east-west) x 1.2^o (north-south) x 75 km (vertical) for altitudes 75-750 km. I adopted objective standards in determining reference curves of TEC from which the anomalies are defined. I regularized the inversion by introducing two different constraints, the continuity constraint and constraints around zero with altitude-dependent allowances. Performances of the 3D tomography have been confirmed by various resolution tests for artificial patterns.

I compare the spatial and temporal distribution of the 3D structure of ionospheric electron density anomalies immediately before these two megathrust earthquakes together with those of another large earthquake (the 2015 M_w 8.3 Illapel) studied by He and Heki (2018). The results of the three cases showed that the preseismic ionospheric anomalies have following common features; (1) they are composed of pairs of low-altitude positive and high-altitude negative electron

density anomalies, (2) they occur above the land area close to the submarine faults, and (3) they have clear onsets a few tens of minutes before earthquakes (~40 min before 2011 Tohoku-oki, and Maule, and ~20 minutes before the Illapel earthquakes) and grow with decaying rates.

I hypothesize the physical process consistent with such 3D structure as follows. Electric fields made by surface positive charges reach the ionosphere. The field generates electromotive forces and makes electrons move down along geomagnetic fields, and this upward current makes eastward/westward magnetic field in regions to the south/north of the epicenter before earthquakes in northern/southern hemisphere. The current will continue until the induced electric field cancels the external field made by surface charges, making the electric potential uniform along the magnetic field. The current will depend on the along-field component of the external electric field and the density of free electrons as a function of altitude. The nonuniform electric currents would result in convergence/divergence of electrons and make positive/negative electron density anomalies at the lower/higher ionosphere along the magnetic field, the structure consistent with those found for these three earthquakes by 3D tomography. I will also compare strengths and dimensions of the electron density anomalies before these three earthquakes and discuss future perspective of preseismic ionospheric anomalies.

Acknowledgments

In the name of Allah, God, the greatest one,

First of all, I praise to Allah subhanahuwata'ala for the things He has given to me. Since in the last three years period of my study, it is not only a journey of achieving a highest degree, but also is becoming my greatest experience ever in my life. Indeed, the second place for all of these, I would acknowledge my parents who have always been supporting and praying for me to go further just for the sake of knowledge. Third place is without a doubt, I thank to my little family (my wife and my children) who have been accompanying and supporting my journey in Japan as well as coloring my new life.

Over the three years, an incredible number of people have been helping me a lot in my journey. They deserve the gratitude of a thousand pages. First, I would like to express my sincere gratitude to Prof. Kosuke Heki, my supervisor, who has given me opportunity to become greater and smarter researcher. I learned many lessons and all of those are really valuable for my carrier path. He taught me about programming with its technical aspects, making a presentation, presenting slides, writing a scientific paper, and gave me chances to speak at international conferences. Sensei inspires me, and I could not have written this thesis without that inspiration. Thanks again sensei as always.

My sincere gratitude to Prof. Masato Furuya, Prof. Kiyoshi Yomogida, Prof. Kazunori Yoshizawa, and Dr. Yoichiro Takada for the advices delivered to my study during weekly solid-earth science seminar or after the seminar. Those are definitely encouraging me to become better

and better in scientific field. Also, my colleagues at Space Geodesy and Seismology Laboratories. I received many new perspectives of earth-sciences after discussing with them.

I thank the Geospatial Information Authority (GSI) for GEONET data (available from terras.gsi.go.jp) and Electric Navigation Research Institute (ENRI) for the inter-frequency bias data for GEONET stations (access www.enri.go.jp or write to Takeyasu Sakai sakai@enri.go.jp to obtain the bias). I also thank Byung-Kyu Choi, Korea Astronomy and Space Science Institute, for the Korean RINEX data files on March 11, 2011. One needs to write to bkchoi@kasi.re.kr to access the Korean data. I thank Dr. He Liming, Northeast University, for helpful comments. It is also grateful to have GIM data from University of Berne, Switzerland. Thanks for providing them.

And finally, I thank to The Ministry of Education, Culture, Sports, Science and Technology (MEXT) who supports me financially during my PhD study in Hokkaido University.

Chapter 1: Introduction

1.1 GNSS for Positioning

The era of precise positioning system available worldwide started by the launches of the global navigation satellite system (GNSS) satellites in late 1980s. The Global Positioning Systems (GPS), maintained by the United States, is the first GNSS with a constellation of satellites orbiting the earth at altitude ~20,000 km. GPS is designed to extract the positions and velocities of moving objects in three-dimensional (3D) space continuously all over the world regardless of weather and time. Such information used to be only for military purposes and closed for civilian services. Nowadays, the technology is available for everyone, thus the position of any objects around the globe can be obtained using various GNSS including GPS.

There are several GNSS newer than GPS. The Russian GNSS, called Globalnoya Navigatsionnaya Sputnikovaya Sistema (GLONASS) is orbiting the earth at altitudes somewhat lower than those of GPS, ~19,000 km above the earth's surface. Galileo (European Navigation System) flies at ~23,000 km altitude whereas some of the Chinese GNSS satellites (Beidou, BDS) and the Japanese navigation satellites (Quasi-Zenith Satellite System, QZSS) employ much higher geostationary and quasi-zenith orbits, respectively. Wherever they are, all the GNSS satellites transmit microwave signals to earth to enable global navigation.

By measuring distances between an object (equipped with a GNSS receiver) and satellites, we can exactly tell where the object is. GNSS satellites transmit digital information about e.g. satellite orbits, clocks, as well as the satellite condition, using two L-band microwave carriers, which are often called L1 and L2 (and sometimes additional L5).

The national datum for surveying and mapping in a country is often maintained by GNSS, for example by building control points with precise GNSS surveying. The latitude and longitude measured by GNSS at one control point are defined on a reference ellipsoid of the earth, and the height can be directly measured relative to the ellipsoid instead of the local mean sea level. The standard ellipsoidal model widely used for GNSS is World Geodetic System 1984 (WGS-84). By establishing ties to reference systems, GNSS has improved the accuracy and consistency with the national datum so that it can be used for further scientific applications.

The microwave signals from GNSS satellites face delays caused by two layers of the earth's atmosphere before they reach receivers on the ground. The first layer is the ionosphere (ionized upper atmosphere) and the second is the troposphere (both water vapor and dry atmosphere). Atmospheric delays that occur in microwaves cause serious positioning errors, and precise positioning by GNSS needs to consider these atmospheric delays in processing the GNSS data. On the other hand, existence of such delays in the microwave signals enables us to study changes in these two layers. This thesis makes use of the atmospheric delays, especially those in the ionosphere, to investigate the dynamics within the ionosphere.

1.2 GNSS for Ionospheric Studies

Total Electron Content (TEC) signifies the number of electrons within a column of 1 m^2 along the signal path in the ionosphere and is expressed with TEC unit (TECU, 1 TECU equivalent to 10^{16} electrons/m^2). It is an integration of electron density, n_e (s) along line-of-sight (LoS) connecting the satellite with the ground receiver as shown in equation (1).

$$TEC = \int_{satellite}^{receiver} n_e(s)ds \quad (1)$$

TEC is a useful quantity to indicate the total amount of free electrons in the ionosphere. A convenient way to measure TEC is to utilize GNSS data, using a technique called GNSS-TEC or GPS-TEC. Further details of the ionosphere and the GPS-TEC technique will be explained later. In comparison with conventional methods like ionosondes, GNSS-TEC method has much better resolution both in space and time in regions where dense GNSS networks are available (Heki, 2021).

GNSS-TEC technique has been playing an important role in studying ionospheric disturbances of space weather origin. Such disturbances include the large scale travelling ionospheric disturbances (LSTID) and medium scale travelling ionospheric disturbances (MSTID) in the mid-latitude region (e.g. Saito, 1998; Otsuka et al., 2011), as well as the sporadic-E, extremely high electron density patches occurring in the E-region of the ionosphere (Muafiry and Heki, 2018).

The GNSS-TEC method has enabled researcher to detect ionospheric disturbances triggered by lithospheric phenomena. For example, those associated with large earthquakes are known as the coseismic ionospheric disturbance (CID) (Calais and Minster, 1995; Heki and Ping, 2005; Cahyadi and Heki, 2015). Acoustic waves excited by coseismic vertical crustal movements propagate upward and disturb the ionosphere as CID. I will further discuss this topic later in the thesis. In addition earthquakes, Heki (2006) detected ionospheric disturbances excited by acoustic waves by a 2004 Vulcanian volcanic explosion of the Asama volcano in central Japan. Kundu et

al. (2021) detected ionospheric disturbances caused by an artificial explosion in 2020 August in Beirut, Lebanon.

1.3 Ionospheric Structure

Ionosphere is the uppermost layer of the earth's atmosphere where significant amounts of neutral gasses are ionized due to solar radiation. Such photoionization produces electrons and positive ions (Kelley, 2009). The ionosphere ranges in altitude from ~80 km up to several hundreds of kilometers. They are divided into the D (~80 km), E (~100 km), and F (higher) regions. The peak electron density occurs at altitude of ~300 km in the F-region (Kelley, 2009). During the night, D and E regions become ambiguous, but they emerge again soon after sunrise.

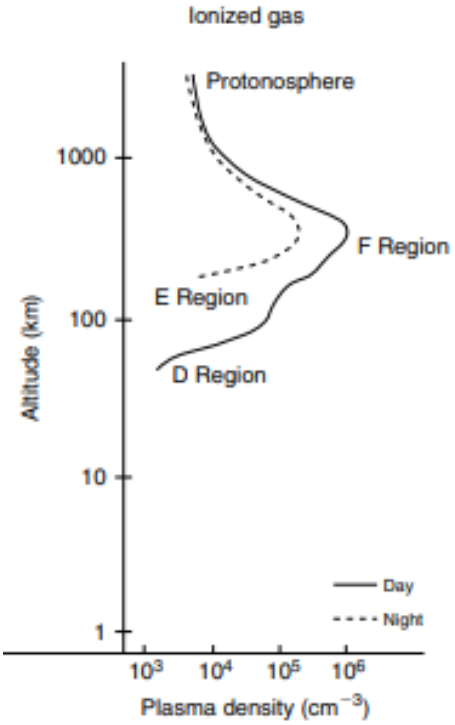


Figure 1. Typical vertical profile of ionosphere (Kelley, 2009)

In 1931, Sydney Chapman, in USA, presented a mathematical model for the formation of ionized layers based on the photoionization processes. He is the first who derived the distribution of ionization as a function of height based on absorption of solar radiation. In Chapter 2.6, I introduce his simple expression of electron production as functions of height and the solar zenith angle. The Chapman function will be used in constraining the solution around zero in the 3D tomography calculations in this study.

The existence of the ionosphere was recognized for the first time when radio waves are realized to propagate over large distances. In 1882, Balfour Stewart in Scotland suggested the existence of an ionized region in the atmosphere by measuring the variation of geomagnetic field using a compass. In 1901, Guglielmo Marconi, Italy, sent radio waves from England to Canada demonstrating that the ionosphere acted like a mirror for high frequency (HF) radio waves.

Ionosphere has been extensively utilized for long-distance radio communications using HF radio waves, which are bounced back to ground and enable global-scale propagation. Higher frequency (e.g. VHF) radio waves penetrate ionosphere and cannot be used for telecommunications. Owing to the usefulness of the ionosphere for public, people have long been monitoring ionosphere with various sensors including ionosondes, satellites, and radars.

I consider that recent discoveries of ionospheric disturbances related to large earthquakes greatly enhanced the implication of the ionospheric studies. Among others, I pick up a recent topic of ionospheric anomalies preceding large earthquakes. Considering a long unsuccessful history of earthquake prediction, TEC changes immediately before large earthquakes found shortly after the 2011 Tohoku-oki earthquake by Heki (2011) could become a key phenomenon toward the

operation of practical earthquake prediction and mitigation of earthquake disasters in the future. I will discuss the link between earthquakes and ionosphere in more detail in Chapter 1.6.

1.4 Solid Earth and Ionosphere

The lithosphere is the uppermost part of the solid earth from the surface (0 km altitude) way down to the depth ~100 km. Lithosphere is divided into tectonic plates, which consist of oceanic and continental plates. The asthenosphere below the lithosphere allows tectonic plates to move around and interact with each other causing variety of phenomena along their boundaries.

There are three types of plate boundaries. The first one is the divergent boundary, i.e., one plate goes away from another plate due to extensional force acting along the boundary. Divergent plate boundaries usually exist in the ocean floor as submarine mountain ranges, such as the Mid-Atlantic Ridge and the East Pacific Rise. The second boundary is the convergent boundary, where the plates collide with each other. Compressional forces between the two plates cause large earthquakes along such convergent boundaries. Such boundaries include the Japan Trench off the Pacific coast of NE Japan, and the Sumatra subduction zone running to the west of the Sumatra Island. Plate convergence often causes mountain building, and an island arcs is formed at one side of the convergent boundary. The last type is the translational plate boundary, where one plate moves sideways along the plate boundary (transform faults). The San Andreas fault zone in the western United States (US) is the typical plate boundary of this type.

Recently, solid earth was found to disturb the ionosphere in several different ways. For example, vertical movement of the surface during an earthquake faulting excites acoustic waves in the atmosphere. This wave propagates upward and reach the F-layer of the ionosphere and

187 makes a N-shaped pulse in TEC (Heki, 2021). This typically occurs ~10 minutes after the
188 earthquake and can be as early as ~8 minutes after earthquake (Astafyeva et al., 2011). This kind
189 of ionospheric anomaly is often called coseismic ionospheric disturbance (CID) and propagates
190 horizontally at the F region sound speed 0.8-1.0 km/s.

191 Since the first detection of CID with GNSS by Calais and Minster (1995), there have been
192 numbers of studies discussing the characteristics and underlying physics of CID. For example,
193 Heki and Ping (2005) showed that the directivity of CID is controlled by the geomagnetic field by
194 studying CID due to the 2003 Tokachi-oki earthquake, Hokkaido, for the first time using a dense
195 network of GNSS. Such a directivity arises because of the Lorentz force acting on the movement
196 of free electrons associated with the propagation of acoustic wave within neutral atmosphere in F-
197 region. In the mid-latitude region in the northern hemisphere, such particle motions become
198 perpendicular with the magnetic field at the northern side of the epicenter resulting in suppression
199 of electron oscillations to the north of the epicenter.

200 Astafyeva and Heki (2009) studied the diversity of the CID waveforms for earthquakes
201 with different focal mechanisms by studying the three large earthquakes 1994, 2006, and 2007
202 with different focal mechanisms in the Kuril Islands. They demonstrated that a normal fault
203 earthquake could give rise to CID starting with a negative change of TEC, in contrast to CID by
204 reverse fault earthquakes starting with positive changes. For these earthquakes, Astafyeva et al.
205 (2009) also identified the co-existence of two different kinds of acoustic waves, i.e., CID due to
206 direct acoustic waves from the epicenter, and those excited by vertical crustal movements
207 associated with the passage of the Rayleigh surface wave. The latter can be distinguished from the
208 former by the propagation speed (~4 km/s) much faster than the former.

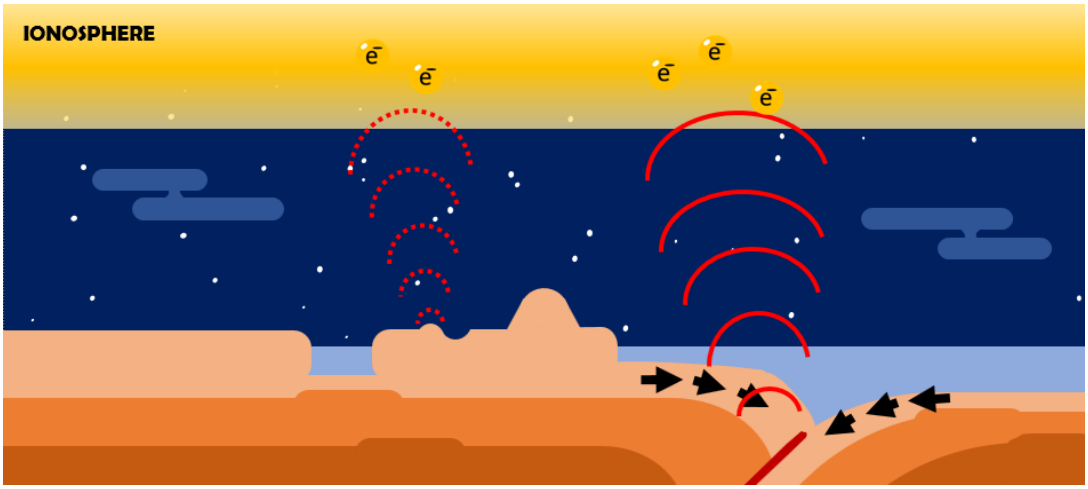


Figure 2. The acoustic wave (red circular wave) excited by coseismic vertical crustal movement may propagate upward and disturb the ionosphere as CID. Surface Rayleigh wave triggers secondary acoustic wave (dashed red circular wave).

The CID by the Rayleigh surface waves has smaller geometric decay allowing the wave to reach farther distance propagation. Heki (2021) shows clear signatures of the Rayleigh wave generated by the 2004 M_w 9.2 Sumatra-Andaman earthquake in GEONET data in Japan ~40 minutes after the main shock. This kind of ionospheric disturbances help us infer surface wave velocities in a region with limited number of seismometers.

1.5 Ionospheric Disturbance due to the Sea Surface Motion

Initial ocean motion generated by subduction zone earthquake causes acoustic disturbance in ionosphere. There, the electron motion constrained by geomagnetic field makes long-lasting electron depletion (formation of an ionospheric hole) above the tsunami source area (Kakinami et al., 2012; Shinagawa et al., 2013; Zettergren and Snively, 2019). Such an ionospheric hole shows TEC decrease right above the region of maximum uplift (due to the meter-scale downwelling of

the sea surface, Figure 3). The anomaly in the ionosphere starts right after the arrival of the acoustic wave and stays above the rupture area with little migration.

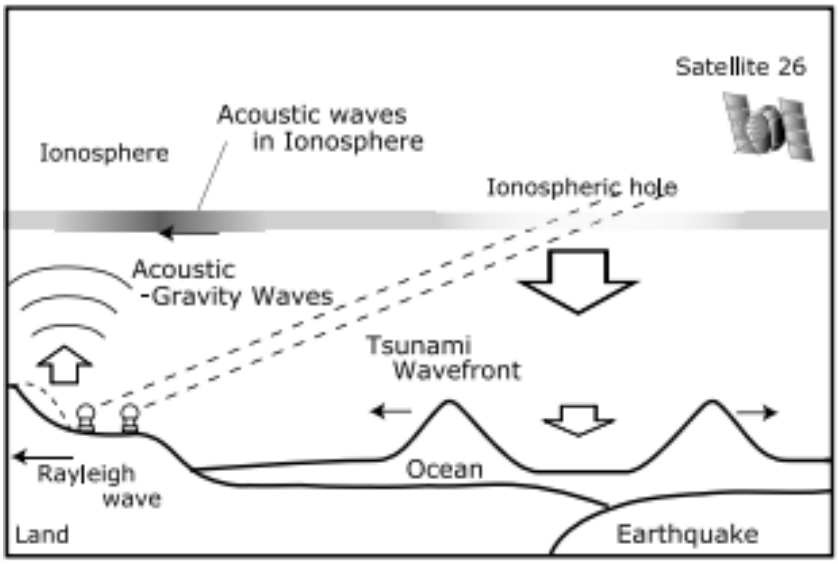


Figure 3. The coupling between ionosphere and sea surface and formation of the ionospheric hole after a large earthquake (Kakinami et al., 2012)

Rolland et al. (2010) found that the tsunami of the 2006 M_w 8.3 Kuril earthquake excited internal gravity waves and subsequent ionospheric disturbances with amplitudes 0.15-0.50 TECU. The tsunami waves generated by the 2004 M_w 9.2 Sumatran-Andaman earthquake also caused similar disturbances in the upper atmosphere above the Hawaiian Islands (Liu et al., 2006). There, the maximum peak-to-trough change was ~0.16 TECU. Such waves were also detected by altimeters on board the Jason-1 and Topex/Poseidon satellites and yielded TEC changes of 0.2-0.6 TECU in 30 seconds (Occhipinti et al., 2006).

1.6 Earthquake Precursors in Ionosphere

Ionospheric precursors of large earthquake are divided into long-term and short-term anomalies. The long-term precursors are detectable more than 1 day prior to the earthquake. Liu et al. (2001) found anomalous diurnal variation of ionospheric TEC from GNSS observations above the epicentral region of the 1999 Chi-chi earthquake (M_w7.7), Taiwan. They showed that the diurnal variation amplitude decreased three to four days before the earthquake. Based on the analyses of many past earthquakes, Le et al. (2011) and Thomas et al. (2017) gave positive and negative conclusions, respectively, on the statistical significance of such precursory changes. On the other hand, the short-term anomaly first found by Heki (2011) occurs immediately before the main shock. This is the phenomenon I discuss in this thesis. For both long- and short-term anomalies, underlying physical mechanisms have remained ambiguous and controversial.

Searches for ionospheric anomalies related to large earthquakes involved satellites orbiting the earth. Using the data from the DEMETER (Detection of Electro-Magnetic Emissions Transmitted from Earthquake Regions) satellite launched by France, Němec et al. (2008) and Li and Parrot (2013) reported statistically significant anomalies in lower ionospheric electron density shortly before earthquakes. Newly launched China Seismo-Electromagnetic Satellite (CSES) has been used to investigate the TEC precursors. Song et al. (2020) found anomalies several days before the 2018 M_w 6.4 Lombok Earthquake. Adopting the moving median method (MMM) to the electron density data, they found precursory electron density enhancements occurred 2-5 days before this earthquake.

1.7 3D Tomography for Ionospheric Electron Density Anomalies

Computerized Tomography (CT) for ionospheric imaging has been developed over the last three decades. It was started by Austen et al. (1988), who tried to demonstrate the feasibility of CT to image ionospheric electron density distributions. He reconstructed two-dimensional (2D) image of electron density using TEC data obtained along the path from the naval navigation satellite systems (NNSS) toward several ground-based receivers. The results demonstrated that CT can be applied to study the ionosphere.

In the last decade, tomographic approaches to the ionosphere has advanced owing to the improved computation techniques and new data sets they used. For example, Tang et al. (2015) presented clear images of the ionosphere in 3D during an ionospheric storm under high geomagnetic activity. They utilized multiple observation techniques including radio-occultation, satellite-borne altimetry, conventional ionosonde, and the GPS-TEC technique.

After that, another ionospheric 3D tomography study was reported by Chen et al. (2016). There, they used only the GPS-TEC data to study the 3D spatial structure of MSTID. Taking advantage of the dense network of the receivers, they could successfully reconstruct electron density irregularities with 3D tomography. As another example, Garcia et al. (2005) imaged coseismic ionospheric perturbation by the Denali earthquake using GPS-TEC data. Although the anomaly was very large in space and GPS stations were not so dense, they could reveal the 3D structure to a certain extent.

Investigation of the electron density distribution in ionosphere is crucial in understanding physical mechanisms of ionospheric disturbances. The computerized ionospheric tomography is

an effective and promising approach to study 3D structures of ionospheric electron density, particularly in the region where dense GNSS networks are available like the Japanese Islands (Seemala et al., 2014; Chen et al., 2016; Saito et al., 2016).

1.8 Research Objectives

This thesis aims to map the ionospheric electron density anomalies related to large earthquakes by using the 3D tomography method and TEC data sets from ground GNSS networks. There are four specific ionospheric anomalies to be investigated here:

1. The ionospheric anomalies prior to the 2011 M_w 9.0 Tohoku-oki earthquake
2. The ionospheric anomalies prior to the 2010 M_w 8.8 Maule earthquake
3. The ionospheric anomalies after the 2011 Tohoku-oki earthquake
4. The ionospheric anomalies after the 2010 Maule earthquake

Then, I will discuss the differences in the preseismic ionospheric anomalies of the 3 different earthquakes, i.e. the 2011 M_w 9.0 Tohoku-oki and the 2010 M_w 8.8 Maule earthquakes studied here, and the 2015 M_w 8.3 Illapel earthquake reported in He and Heki (2018). I finally discuss physical mechanisms for the short-term precursory changes in ionosphere, based on the 3D tomography results obtained in this study.

Chapter 2: Data and Method

2.1 GNSS Network in Japan

Geospatial Information Authority of Japan (GSI) operates the nationwide dense GNSS-network that covers the Japanese archipelago with ~1,300 stations with an average interval of ~20 km. This network is used to study crustal deformation and to serve as "electronic reference points" in local geodetic surveys in Japan. This nationwide GNSS array is called GEONET (GNSS Earth Observation Network). The raw observation data and daily coordinates of the GEONET station are open to public on-line (terras.gsi.go.jp) in Japan. The raw data files in the receiver-independent exchange (RINEX) format provide data with the 30 second sampling interval. In this study, I downloaded the RINEX files from all the GEONET stations available for the studied dates.

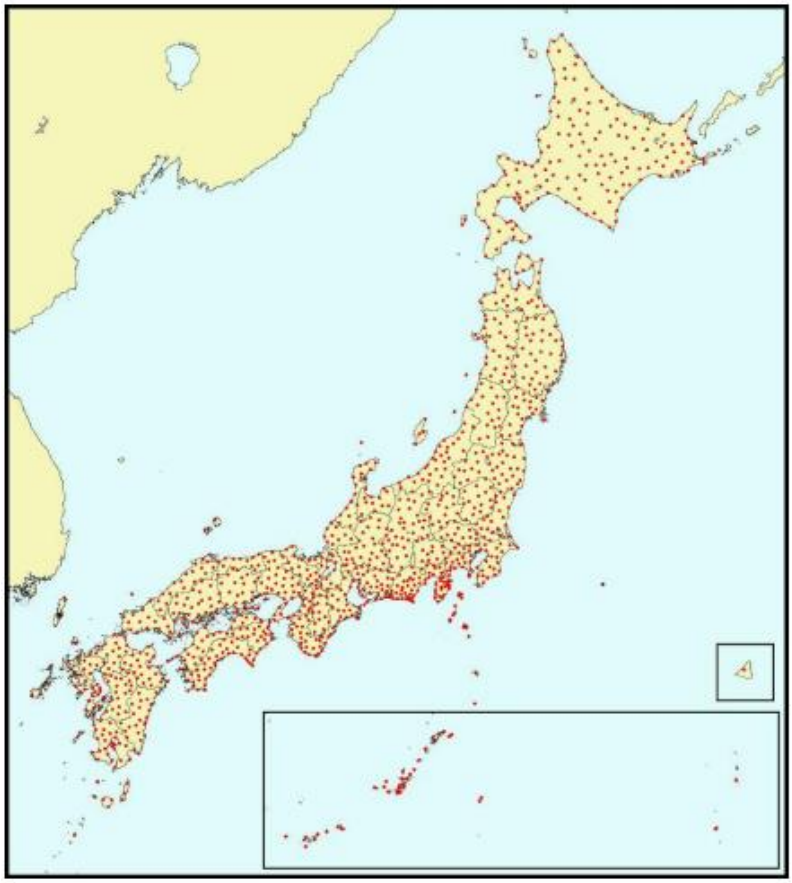
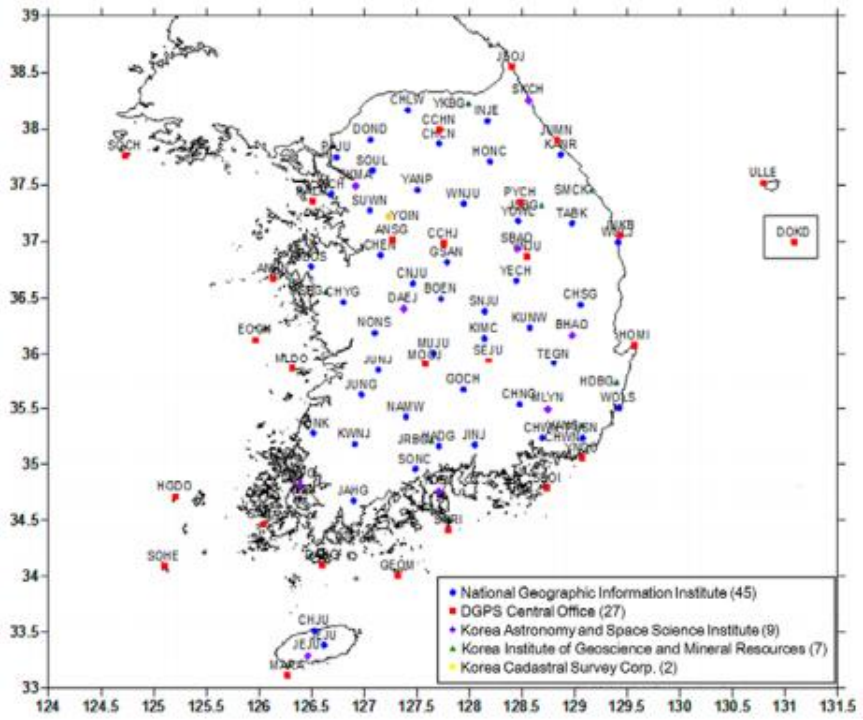


Figure 4. ~1,300 GEONET stations (red dots) are available in Japan (Tsuji and Hatanaka, 2018)

2.2 GNSS Network in South Korea

National Geographic Information Institute (NGII) of South Korea operates Korean GNSS Network (KGN) that covers the South Korea with over 45 stations with separations of 20-50 km. This network has been operated since March 1995 to investigate crustal deformation in the Korean Peninsula and its vicinity and serves as the national datum for precise positioning system (Kwon, 2012). The raw GNSS data in the RINEX format files are recorded with the time interval of 30 seconds (Choi and Hong, 2019).



316

317 **Figure 5.** The dense GNSS network in South Korea (Kwon, 2012)

318 In this study, 53 stations of the Korean GNSS network are used for studying the ionospheric
319 anomalies before and after the 2011 M_w 9.0 Tohoku-oki earthquake. Although the target of this
320 study is ionosphere above the Tohoku region (far away from Korea), the availability of far-field
321 station for this study is important to reinforce the spatial resolution of the 3D tomography of the
322 ionosphere, especially in the western part of studied area.

323

324

2.3 GNSS Networks in South America

The RINEX data used in this study for South America are obtained from several different organizations including the Centro Sismológico Nacional of Universidad de Chile, the Red Argentina de Monitoreo Satelital Continuo (RAMSC) network of Instituto Geográfico Nacional de Argentina (IGNA), the Rede Brasileira de Monitoramento Contínuo dos Sistemas GNSS (RBMC) network of Instituto Brasileiro de Geografia e Estatística (IBGE), International GNSS Service (www.igs.org), and University NAVSTAR Consortium (www.unavco.org).

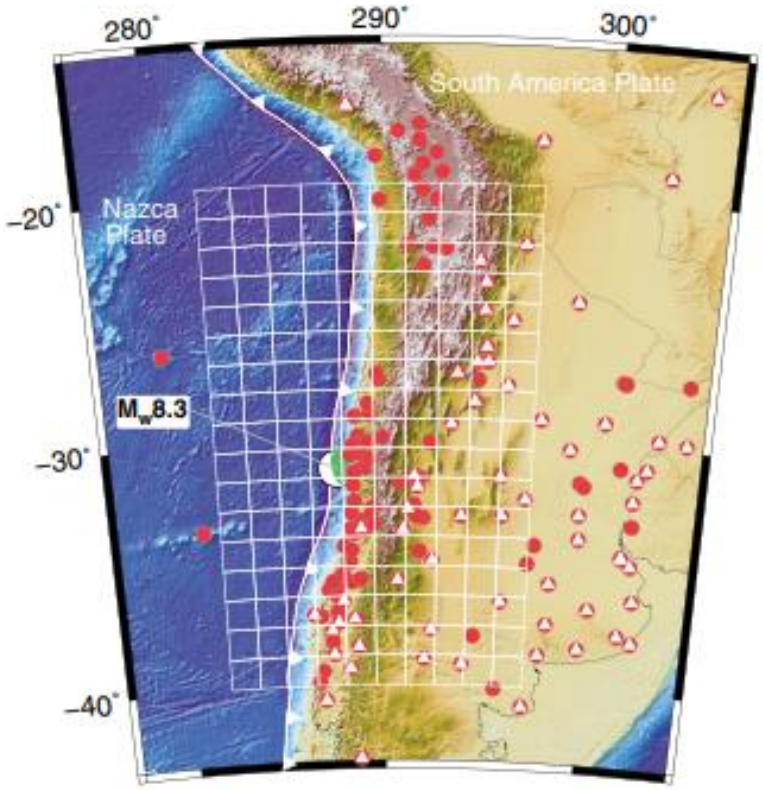


Figure 6. 146 GNSS stations in South America used by He and Heki (2018) for 3D ionospheric tomography of ionospheric anomalies before the 2015 Illapel earthquake.

There are 146 GNSS stations in South America and 65 of them can track GLONASS as well as GPS. These data are used to analyze the TEC changes before the 2015 M_w 8.3 Illapel, and 89 of those GNSS stations were used to study the 2010 M_w 8.8 Maule earthquakes.

2.4 GNSS-TEC Method

The slant TEC (STEC) is observed for a pair of GNSS satellite and receiver and corresponds to the total number of electrons integrated along the line-of-sight (LoS). The STEC is derived from the change in the phase differences ΔL4 between the L1 and L2 microwave carrier phases (expressed in length). In this study, equation (2) is used to convert L4 changes into STEC changes:

$$\Delta\, STEC = \left(\frac{1}{40.308}\right) f_1^2 f_2^2 / (f_1^2 - f_1^2) \Delta L_4 \quad (2)$$

There, f_1 (1575.42 MHz), f_2 (1227.6 MHz) are the frequencies of the two carrier waves (L1 and L2) in the L-band from GPS satellites, respectively (such frequencies are slightly different for other GNSS). The phase difference of the two frequencies (ΔL4) are often called the ionospheric linear combination or geometry-free linear combination. The coefficient 40.308 is to convert ionospheric delays into TEC in TEC unit (TECU, 10^{16} electrons/m^2).

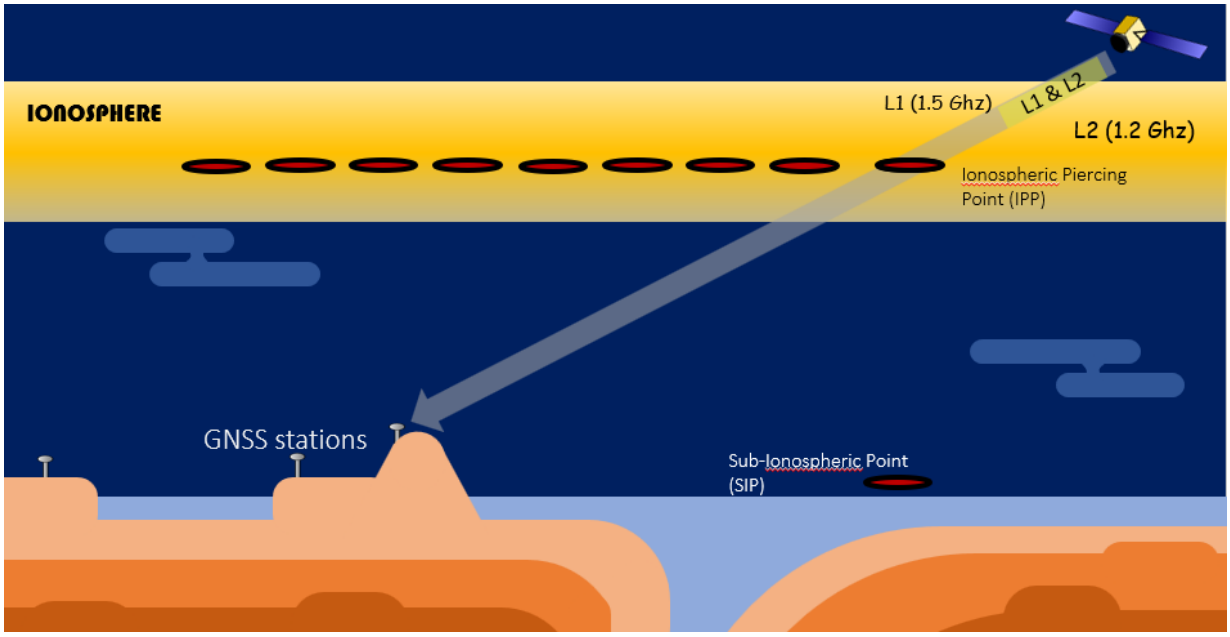


Figure 7. Illustration of L1 and L2 microwave signals propagating from GNSS satellites to GNSS receivers. IPP is the intersection of LoS with the hypothetical thin layer in ionosphere, and its ground projection is called SIP.

When GNSS satellites transmit microwave signals in both L1 and L2 frequencies, LoS will have an intersection point with the ionosphere. This intersection is called as ionospheric pierce point (IPP) and its projection onto the earth surface is named as sub-ionospheric point (SIP). Although the actual ionosphere is distributed over a wide range of altitudes, we assume a thin hypothetical layer at the height of largest electron density (~300 km) to calculate IPP and SIP coordinates, usually expressed with the geocentric cartesian coordinates fixed to the solid earth. There are 32 GPS satellites at this moment, and the number of satellites have been increasing drastically by the development of GNSS other than GPS. The increase of numbers of ground stations and GNSS satellites is important in the performance of the 3D tomography technique used in this study.

We need to remove the satellite and receiver inter-frequency biases (IFB) caused by different electric path lengths of L1 and L2 circuits within satellites and receivers. For the GEONET stations, such biases can be downloaded from Electric Navigation Research Institute (ENRI) website (www.enri.go.jp) (Sakai, 2005). After correcting for these biases, we can convert STEC to vertical TEC (VTEC) by multiplying them with the cosine of the incidence angle of LoS to ionosphere. For the stations in South Korea and South America, the receiver biases are determined by minimum scalloping method by Rideout and Coster (2006). In this method, a receiver IFB of a certain station is obtained by minimizing the scatter of VTEC during a period from midnight to dawn obtained with various satellites observed at that GNSS station. Satellite IFBs are obtained from the header information of the Global Ionosphere Maps (GIM) downloaded from University of Berne (aiub.unibe.ch/CODE).

I first isolated the absolute STEC by removing IFBs. Then, such STEC is converted to VTEC by multiplying it with the cosine of the incident angles of LoS with a thin layer at 300 km altitude. I use equation (3) to calculate VTEC:

$$\mathrm{VTEC} = (\mathrm{STEC} - d)cos\theta, \quad (3)$$

where θ and d represent the incidence angle of LoS at IPP altitude, and IFB (sum of satellite IFB and receiver IFB) for this satellite-receiver pair, respectively. Such VTEC data do not contain apparent U-shaped changes caused by elevation angle variations and are much easier to interpret than STEC.

2.5 Strategies to Isolate Anomalies from GNSS-TEC Data

In this study, I use TEC changes obtained from the time series of VTEC. Anomalous behavior of VTEC needs to be extracted from the observed data. Here I adopt the following two types of strategies to isolate the ionospheric anomalies:

1. Modelling the temporal change of VTEC with a polynomial of time which is estimated using the least-squares method. For example, if the polynomial degree is two, the model is expressed by equation (4):

$$\mathrm{VTEC}\ (t) = at^2 + bt + c, \tag{4}$$

where *a*, *b*, and *c* are parameters to be estimated using the least squares method. The estimated models will serve as reference curves, and differences from these curves are defined as the anomalies. There are two key factors we need to care when we obtain the most appropriate models. First one is the choice of the polynomial degree. I use the L-curve method to choose the best degree, i.e., I compare the root-mean-squares of the residuals and employ the degree with which the residual showed a large drop (and insignificant drop for higher degrees). Second factor is the start and the end of the exclusion time window to avoid the leakage of the earthquake-related anomalies into the reference curves. Proper selection of the windows is important to avoid artificial anomalies. I will discuss these two factors in more detail in the next chapter.

2. Making the difference between medians of VTEC from two periods (before and after the start of the anomalies). I use this method when it is difficult to estimate reference curves in an objective manner. Further explanation to this topic will be discussed later.

In this study, I use the first strategy when I analyze preseismic ionospheric changes for the 2011 M_w 9.0 Tohoku-oki, 2015 M_w 8.3 Illapel, and the 2010 M_w 8.8 Maule earthquakes. On the other hand, the second strategy is used to isolate the postseismic electron depletion of the 2011 M_w 9.0 Tohoku-oki earthquake. Each strategy is used to obtain ionospheric anomalies as VTEC residuals. In this study, such VTEC residuals are converted back to STEC residuals and are used as the input to the 3D tomography calculations.

2.6 Ionospheric 3D Tomography Method

The first step to perform 3D tomography is to set up voxels covering the studied region and the target altitude range. The electron density anomaly within a block is assumed homogeneous, and such anomalies are estimated for all the voxels. I employ different setting of voxels for different earthquake cases considering the anticipated region of the anomaly signals and the GNSS station distribution. Smaller voxels would result in a better spatial resolution of the results. However, dense distribution of LoS penetrating the blocks is needed to make the tomography results meaningful.

Thus, the second step is to collect as many LoS passing through the blocks as possible. If the ground GNSS stations track multi-GNSS, i.e., not only GPS but also GLONASS, Galileo and QZSS, such data should also be used as the input to the tomography. In fact, Muafiry et al. (2018) used both GPS and GLONASS data to perform 3D tomography of sporadic E irregularities.

TEC anomaly of an LoS (y_i) from a certain satellite to a certain receiver is composed of the sum of the products of the electron density anomalies (L_j for the j-th block) and the penetration lengths (A_{ij}) for blocks located along the LoS as expressed by equation (5).

$$y_i = \sum_j A_{ij} L_j + e_i \quad (5)$$

There, e_i represents the measurement error of the *i*-th pair, and I assumed it as 0.05 TECU for all the measurements. This corresponds to a typical error for differential GNSS VTEC measurements (Coster et al., 2013). Equation (5) serves as the observation equation and the matrix A_{ij} becomes the Jacobian matrix.

First, I need to calculate the penetration lengths of LoS with voxels (A_{ij}) using simple geometric calculations. Generally speaking, one LoS has two (penetrated) or zero (not penetrated) intersection points with the surface of one voxel, and L_j is the distance between the entry point to the exit point for penetrated voxels. I use the GNSS station positions available in the header information of the RINEX files. The instantaneous satellite coordinates are calculated using the broadcast orbit information of the GNSS satellites. Then, the coordinates of the intersection points of LoS with the block surfaces can be calculated. Let *x*, *y*, z be the coordinate of points along a certain LoS, they can be expressed as follows:

$$x = x_a + \varepsilon (x_s - x_a) \quad (6)$$

$$y = y_a + \varepsilon (y_s - y_a) \quad (7)$$

$$z = z_a + \varepsilon (z_s - z_a) \quad (8)$$

where x_a, y_a, z_a represent the receiver coordinate x_s, y_s, z_s represent the satellite coordinate. The parameter, ε, changes over a range from zero to one ($0 < \varepsilon < 1$), i.e., (*x*, *y*, *z*) signify the receiver and satellite coordinates when ε is 0 and 1, respectively. Coordinates of points on the up-down,

east-west, and north-south surfaces of the block should satisfy the following three equations, respectively.

$$x^2 + y^2 + z^2 = (R + H)^2 \quad (9)$$

$$\frac{y}{x} = \tan \varphi \quad (10)$$

$$\frac{z^2}{(x^2+y^2)} = \tan^2 \theta \quad (11)$$

There, R is the radius of the Earth at this latitude, H, φ, θ are the height, longitude and latitude of the horizontal, vertical (north-south), vertical (east-west) surfaces of a block. Here I assumed that the earth is a sphere without flattening. The coordinates of the LoS penetration points with these surfaces could be obtained by substituting x, y, z in (9)-(11) with those in (6)-(8), and solving for the parameter ε.

Now, the elements of the Jacobian matrix (A_{ij}) in equation (5) has been obtained, and I will proceed to estimate the set of parameters L_j to obtain the electron density anomalies within individual voxels. The observation equation (5) can be written in a matrix form as:

$$\boldsymbol{y} = \mathbf{A}\boldsymbol{x} + \boldsymbol{e} \quad (12)$$

where $\boldsymbol{y}$ is the vector composed of STEC anomalies y_i, $\mathbf{A}$ is the Jacobian matrix composed of A_{ij}, $\boldsymbol{x}$ is the vector composed of unknown parameters x_j (electron density anomalies of individual blocks), and $\boldsymbol{e}$ is the measurement errors. The vector $\boldsymbol{x}$ is derived by solving the normal equation:

$$\boldsymbol{x} = (\mathbf{A}^T \mathbf{A})^{-1} \boldsymbol{A}^T \boldsymbol{y} \quad (13)$$

after the Cholesky's decomposition, i.e., by decomposing the normal matrix $\boldsymbol{A^T A}$ into lower triangular matrix $\boldsymbol{L}$ and its transpose.

$$\mathbf{A}^{\boldsymbol{T}}\,\mathbf{A} = \boldsymbol{L}\,\boldsymbol{L}^{\boldsymbol{T}} \tag{14}$$

Even if the LoS are densely distributed, they may not penetrate all the blocks, especially above the oceanic and above areas without sufficient stations. Hence, certain constraints need to be introduced to regularize the least-squares inversion. Here, a continuity constraint is used, i.e., it is assumed that neighboring blocks have the same electron density anomalies with a certain allowance for the difference. Suppose block number *j* is at the east side of block number *i*, then assuming x_i and x_j, the electron density anomalies of these blocks, satisfy $x_i - x_j = 0$. One block normally has six neighboring blocks (up, down, north, south, east, and south), and all these pairs are added to the normal matrix as virtual observations (Nakagawa and Oyanagi, 1982). The block pairs that are not juxtaposed is not constrained. I used the allowance for this constraint of 0.10 x 10^{11} el/m^3 (this unit is equivalent to 1 TECU, or 10^{16} electrons/m^2, for penetration length of 100 km).

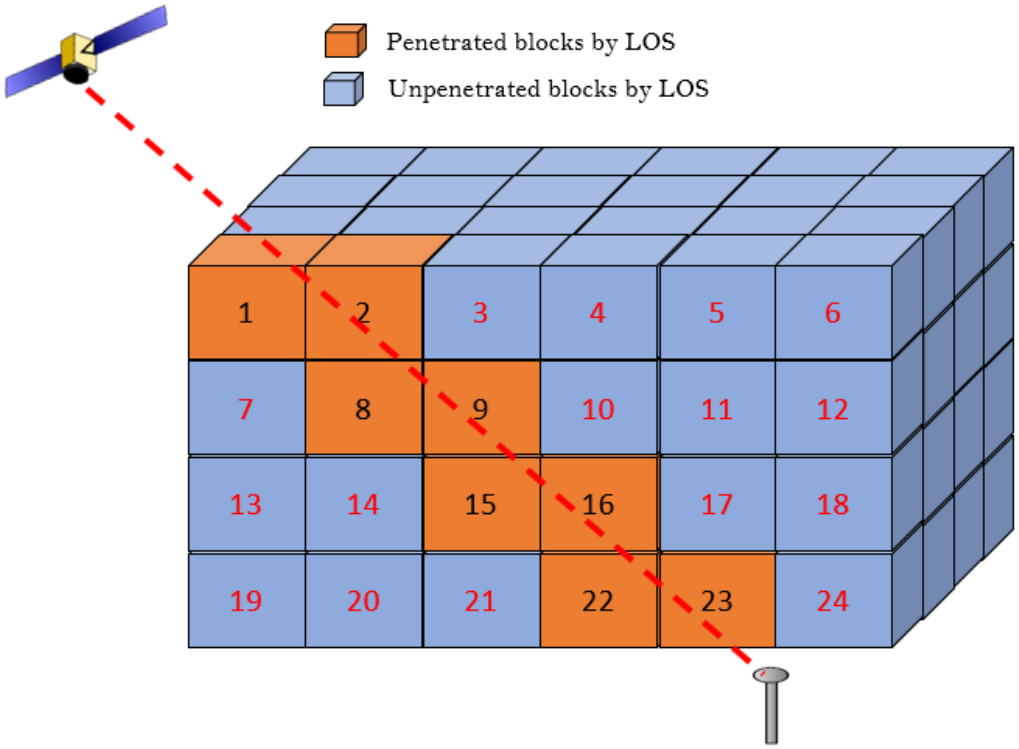


Figure 8. Illustration of blocks (voxels) in 3D tomography and penetration of LoS with a part of the blocks.

As an additional constraint, I weakly constrained the electron density anomalies around zero with an altitude-dependent allowance. According to the Chapman distribution, electron density at height h is proportional to exp $(1 - A - e^{-A})/2$, where A equals to $(h-h_{max})/H$. There, h_{max} is the electron density peak altitude (300 km) and H is assumed 80 km. The allowance for this second constraint was assumed to be proportional to this distribution, and set as large as 1 % of the electron density at that altitude. This implies that I constrain the electron density strongly around zero for altitudes in the D and E regions, where electron density is lower, and weakly

around zero in the F region of the ionosphere, where electron density is higher. This is to avoid estimation of unrealistically large electron density anomalies in very high or very low altitudes.

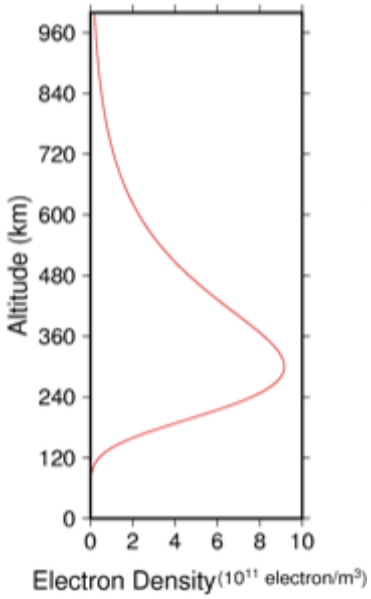


Figure 9. The Chapman functions showing altitude dependence of ionospheric electron densities.

Chapter 3: 3D Tomography of the Ionospheric Anomalies immediately before Earthquakes: The 2011 Tohoku-oki Earthquake

The content of this chapter was published in Journal Geophysical Research Space Physics, Muafiry, I.N.and K. Heki, 3D tomography of the ionospheric anomalies immediately before and after the 2011 Tohoku-oki (M_w9.0) earthquake, J. Geophys. Res. Space Phys., 125, e2020JA027993, doi:10.1029/2020JA027993, 2020

500 **3.1 Introduction: History of Debate**

501 Differential ionospheric delays (phase advances) of the two microwave carriers from
502 GNSS satellites enable us to study ionospheric TEC and its change in high temporal and spatial
503 resolutions. TEC data represents the number of electrons integrated along the LoS connecting
504 satellites and ground receivers. Vertical crustal movements associated with large earthquakes
505 trigger direct acoustic waves propagating upward. They reach the F-region of the ionosphere 8-10
506 minutes after earthquakes and disturb ionosphere causing changes in TEC.

507 Such a coseismic ionospheric disturbance (CID) has been first studied with GNSS by
508 Calais and Minster (1995) and with a dense GNSS network by Heki and Ping (2005). Later,
509 Astafyeva et al. (2011) studied immediate ionospheric response to the 2011 Tohoku-oki
510 earthquake, and Rolland et al. (2013) clarified mechanisms of several important properties such as
511 the CID directivity. Cahyadi and Heki (2015) proposed an empirical law connecting the earthquake
512 magnitude and the CID amplitudes, and Astafyeva and Shults (2019) explored the way to study
513 smaller earthquakes with CID. As reviewed in Heki (2021), the Japanese dense network GEONET
514 (GNSS Earth Observation Network) produces TEC data with high spatial (~20 km) and temporal
515 (30 s) resolution and contributed to our understanding of ionospheric disturbances related to
516 earthquakes.

517 Shortly after the 2011 March 11 Tohoku-oki (M_w9.0) earthquake, Heki (2011) reported the
518 occurrence of positive (and partly negative) changes in TEC starting ~40 minutes before the
519 earthquake near the epicenter using GEONET. Heki (2011) also reported the occurrences of
520 similar anomalies before the 2004 Sumatra-Andaman (M_w 9.2), 2010 Maule (M_w 8.8), and the
521 1994 Hokkaido Toho-oki (M_w 8.3) earthquakes.

Then three papers published after that (Kamogawa and Kakinami, 2013; Utada and Shimizu, 2014; Masci et al., 2015) doubted the reality of the TEC changes before the 2011 Tohoku-oki earthquake. Coseismic acoustic disturbance makes not only short-term N-shaped TEC changes but also airglow (Inchin et al., 2020) and long-lasting electron depletion in the ionosphere (Kakinami et al., 2012; Shinagawa et al., 2013; Zettergren and Snively, 2019). In Heki (2011), the TEC anomalies were defined as the departure from the reference curves. The major criticism by these three papers is that the enhancement is an artefact that emerged by using the data after the earthquake (including the long-lasting TEC drop) in defining the reference curves.

Rebuttals to those three papers have been published in the same journal (Heki and Enomoto, 2013; 2014; 2015). For example, Heki and Enomoto (2015) showed the reality of the positive bending of TEC before earthquakes using the Akaike information criterion (AIC). They confirmed statistical significance of the bending immediately before large earthquakes (e.g. 40 minutes before the 2011 Tohoku-oki earthquake), demonstrating that such bending could be detected even without using the data after earthquake occurrences. They further demonstrated that the leading times and the intensities of the bending depend on M_w from seven large earthquakes with reasonable amount of available GNSS data.

In a mean time, a new algorithm to detect such preseismic TEC changes was proposed by focusing the spatial correlation of preseismic TEC data (Iwata and Umeno, 2016). This work, together with Heki and Enomoto (2015), substantiate the existence of the preseismic anomalies. Subsequently, He and Heki (2017) lowered the threshold of earthquake magnitudes and compiled similar TEC enhancements prior to 18 earthquakes worldwide with M_w 7.3-9.2 and confirmed

543 systematic M_w dependence of preseismic ionospheric anomalies, i.e. the anomalies for earthquakes
544 of larger M_w start earlier and grow stronger (relative to background TEC).

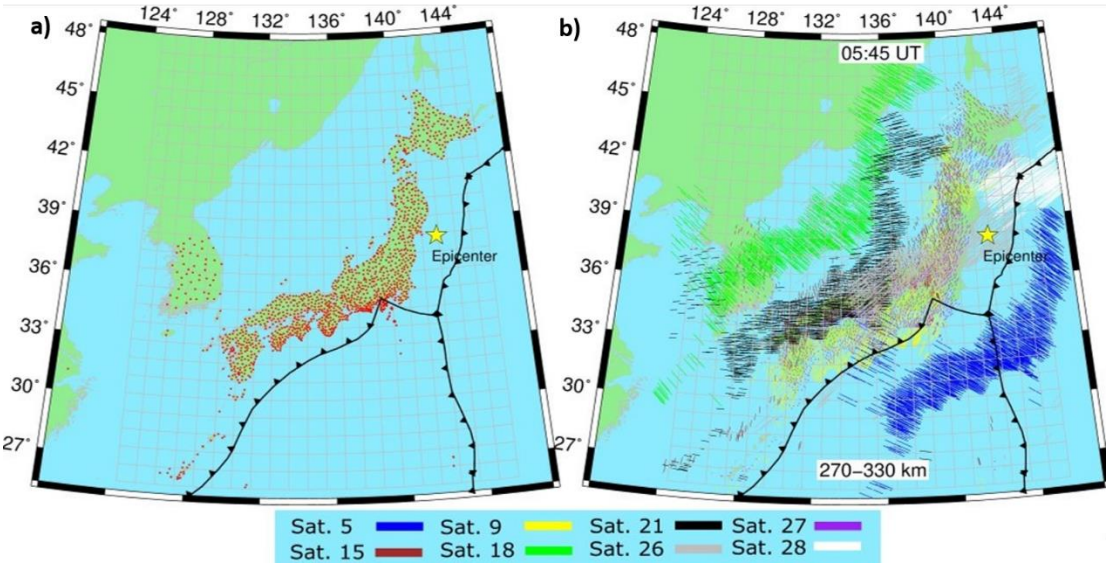
545 The physical mechanism responsible for these preseismic signals is only partly understood.
546 Evidences obtained so far suggest it electromagnetic, assuming e.g. positive surface charges
547 responsible for the ionospheric electron redistribution. Mobile positive holes generated by the
548 breakage of the peroxy bonds that are ubiquitous in rocks (Freund, 2011) offer a scenario consistent
549 with the TEC observations. The holes are a quantum mechanical state and spread as fast as a few
550 hundreds of meters per second from seismogenic depths to the surface (Freund, 2013). Regarding
551 the ionospheric electron redistribution by surface charges, several mechanisms have been
552 proposed, e.g., Kuo et al. (2014) and Kelley et al. (2017). This issue will be discussed in detail
553 later.

554 To understand the underlying physical process, it is effective to investigate the spatial
555 structure and temporal evolution of the preseismic electron density anomalies. Recently, He and
556 Heki (2018) studied the spatial structure of the electron density anomalies before the 2015 Illapel
557 earthquake, Chile (M_w 8.3), using 3D tomography technique. The result suggested that the
558 preseismic changes were composed of two parts, ionosphere electron density increase and
559 decrease. They emerged ~20 minutes before earthquake and are situated at lower and higher
560 altitudes, respectively, along the geomagnetic field. The same 3D tomography technique has been
561 applied for studies of 3D structures of electron density changes by the 2017 total eclipse in North
562 America (He et al., 2018) and sporadic-E irregularities in Japan (Muafiry et al., 2018).

In this study, an improved version of the 3D tomography technique is applied to anomalies immediately before the 2011 Tohoku-oki earthquake. The explanation about our 3D tomography method is explained in detail in Chapter 2. Here, the anomaly signals are stronger than the 2015 Illapel earthquake and would help us better understand the 3D structure and the evolution of the ionospheric electron density anomalies. The leading time of the preseismic anomaly of the 2011 earthquake is longer (~40 minutes) than the 2015 earthquake (~20 minutes). This makes us select the objective procedure to isolate the TEC anomalies carefully, and this issue has been partly discussed in Chapter 2 and will be discussed again later on. At the end of Chapter 3, a simple mechanism to redistribute ionospheric electrons by surface charges is also proposed.

3.2 Data set

GNSS data from the entire GEONET is used, a dense array of continuous GNSS receiving stations in Japan. I also add data from the GNSS network in South Korea, with 53 stations and ~40 km average separation (Choi and Hong, 2019), to reinforce the resolution in the western part of the studied area. In total, I used 1,284 GNSS stations to study the preseismic anomalies of the 2011 Tohoku-oki earthquake (Figure 10a). I used 8 GPS satellites (PRN 05, 09, 15, 18, 21, 26, 27, 28) visible from the studied region immediately before the mainshock (05:45 UT). Unfortunately, GEONET did not track GNSS other than GPS in 2011. Other data set has been explained in detail in Chapter 2.



582

583 **Figure 10.** Maps showing the GNSS station distribution (red dots) and the voxels for 3D
584 tomography above Japan, the Sea of Japan, and the Eurasian Continent including the Korean
585 Peninsula (a). Yellow star indicates the epicenter of the 2011 Tohoku-oki (M_w9.0) Earthquake.
586 Black curves illustrate boundaries between tectonic plates in and around the Japanese Islands. The
587 short lines indicate the LoS of satellite-station pairs at the altitude 270-330 km (one layer of voxels)
588 one minute before the earthquake (b). Color of the lines indicates satellite numbers.

589 **3.3 Data Processing Strategy**

590 As described in Chapter 2, the study of preseismic anomaly will be using reference curves
591 to isolate the VTEC anomalies. This method has been often criticized by two reasons, (1)
592 postseismic drops influence the reference curves and cause artificial enhancements, and (2) it is
593 inappropriate to use the TEC data after the earthquake for earthquake prediction studies. As for
594 (1), I avoid the influence of the postseismic drop by excluding the part of VTEC time series when
595 SIP (the ground projection of the intersection of LoS with a thin layer at 300 km altitude) is above
596 the focal area (see Figure 11 inset maps). Considering the mechanism of postseismic TEC drops
597 by downward plasma transport and recombination (Kakinami et al., 2012; Shinagawa et al., 2013)
598 and numerical simulation of its long-term behavior (Zettergren and Snively, 2019), it is unlikely

599 that the area of postseismic drop occurs in areas far from the focal area, and its influence can be
600 mostly avoided by excluding VTEC data with SIP overlapping the focal region. This will be
601 discussed again later in this section.

602 Regarding (2), a series of studies on this topic, from Heki (2011) to this thesis, do not aim
603 at practical earthquake prediction by observing GNSS-TEC in a near future. It would be more
604 important to answer the question if earthquakes know their final sizes when they start (i.e. the
605 question whether earthquakes are predictable or not) at this moment. From this point of view, rhe
606 reference curve method is appropriate to study preseismic signals because earthquakes would not
607 leave permanent changes (like coseismic steps in station coordinates) in TEC.

608 There are numbers of difference in the method to obtain the TEC anomalies from the early
609 study (Heki, 2011). Here I explain the three main differences, (1) input data, (2) selection of
610 exclusion windows, and (3) determination of polynomial degrees. For point (1), biased STEC is
611 converted to absolute VTEC beforehand and the reference curves are estimated to model the
612 absolute VTEC time series as explained in Chapter 2. This is different from Heki (2011), where
613 both polynomial coefficients and the bias are estimated simultaneously using STEC time series as
614 the input data. The new method enables us to model the time series using higher order polynomials
615 and to optimize the polynomial degrees using the L-curve method.

616 Another difference is that here I include the satellites that do not show significant
617 anomalies. For example, GPS Sat.18 was not studied in Heki (2011) because they showed little
618 TEC anomalies. However, such data are important to show where preseismic anomalies do “not”
619 emerge. After all, I used 8 GPS satellites including four new satellites 5, 18, 21, and 28 in addition

to 9, 15, 26, and 27 studied in Heki (2011). In Figure 12a-d, I show time series, similar to Figure 11, of four examples with these new satellites. There I fit the data with polynomials with degrees determined by the L-curves in the insets. The geometry of the station position, satellite SIP track (calculated assuming 300 km as the height of the thin ionosphere), and the epicenter are given in inset maps. Satellites 18 (c) and 21 (d) do not show significant preseismic anomalies (only coseismic acoustic disturbances) although the excluding windows are used in the polynomial fitting. The data from Satellites 5 (a) and 28 (d) include weak preseismic anomalies together with coseismic acoustic disturbances. These LoS do not penetrate the postseismic negative anomaly and do not show postseismic TEC drops.

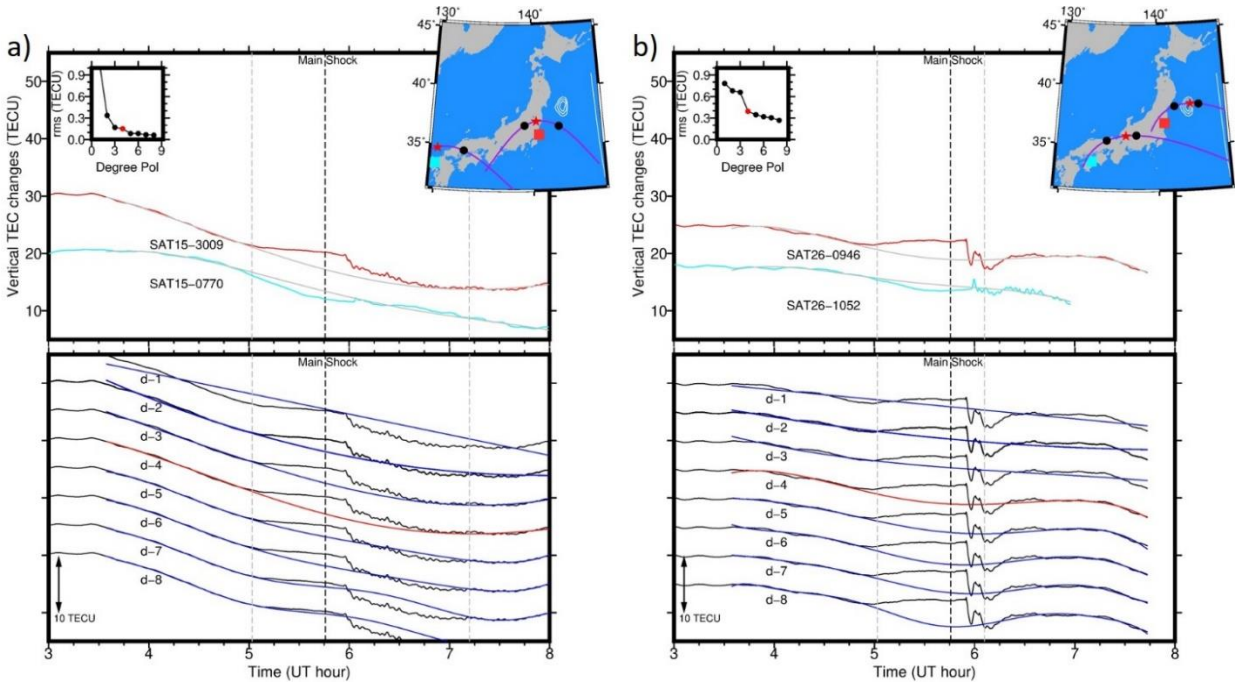
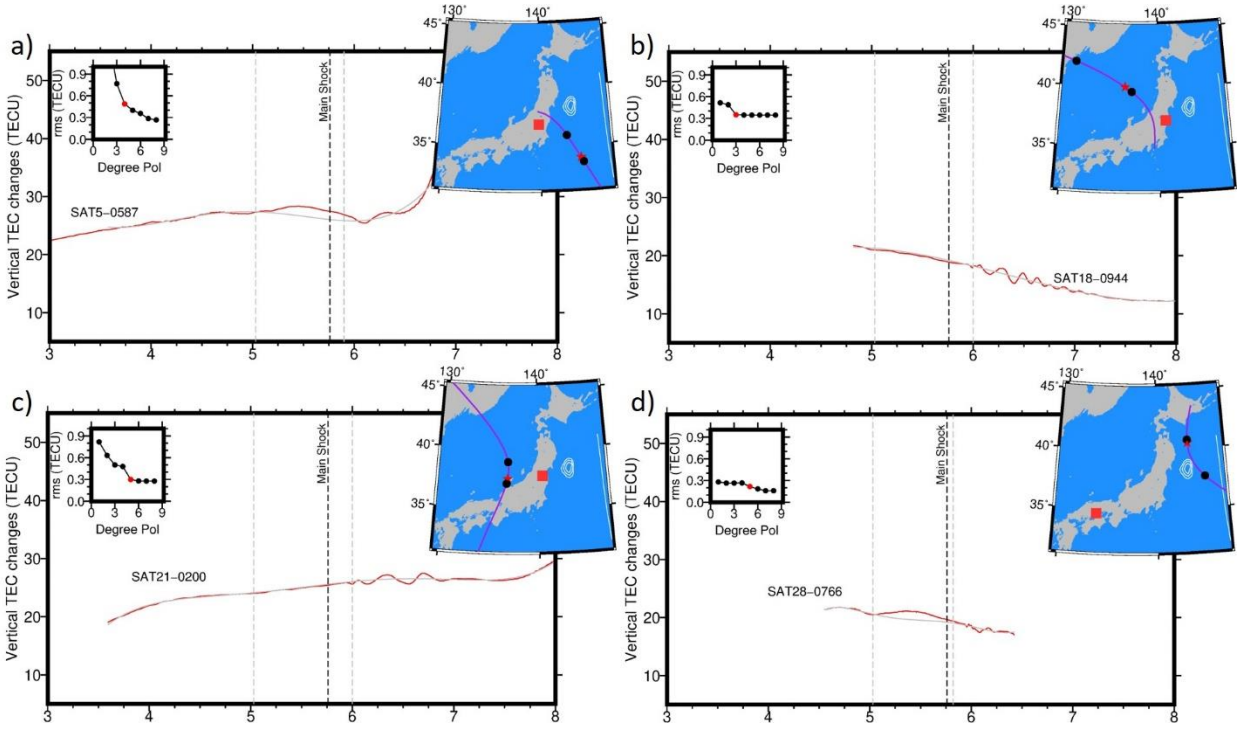


Figure 11. Fitting reference curves of VTEC changes for satellite-receiver pairs of GPS Sat.15-3009 (a) and Sat.26-0946 (b) showing positive preseismic anomalies (upper panel, red curves). I also show two different pairs showing negative anomalies for comparison (upper panel, cyan curves). Vertical dashed lines indicate the exclusion window in fitting the model with polynomials. Red stars and black circles attached to the SIP tracks in the inset maps show the SIP positions at the main shock and at the start and end of the exclusion window (I assumed 300 km to calculate the SIP positions). Red and cyan rectangles indicate the locations of the two receivers. The maps also include the coseismic slip distribution drawn with the contours of 3-meters step (Ozawa et al., 2011). The L-curves in the left insets show the root-mean-square (rms) of the VTEC residuals obtained by fitting curves of various polynomial degrees. I employed the red curves in the lower panels, i.e. degree 4 for (a) and (b), that showed significant rms drops in the L-curves.



642

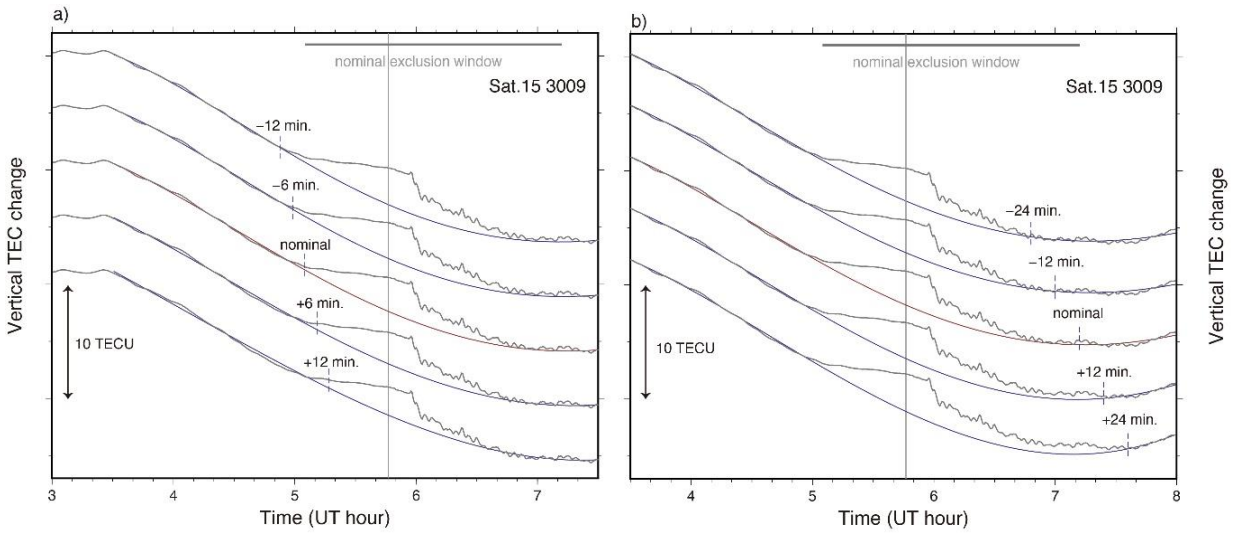
643 **Figure 12.** VTEC time series (red curves) and models with polynomials (grey curves) for satellite-
644 receiver pairs with four newly used GPS satellites, i.e. Sat.5-0587 (a), Sat.18-0944 (b), Sat.21-
645 0200 (c), and Sat.28-0766 (d). See the caption of Figure 11 for other symbols.

646

647 Regarding point (2), Heki (2011) excluded a time window 5.2-6.0 UT possibly influenced
648 by the pre-, co-, and postseismic ionospheric disturbances in fitting the reference curves for all the
649 four satellites. Here, I fit the polynomial to absolute VTEC using the excluding windows with the
650 start and end times determined from external information. The selection of the end of this exclusion
651 window is especially important because reference curves estimated using the period influenced by
652 the long-lasting postseismic TEC drop may give rise to artificial preseismic TEC increase. In
653 Figure 13, I demonstrate that the VTEC anomalies during the preseismic period 5:05-5:46 UT is
654 not so sensitive to the excluding window settings using the case of Figure 2a.

For the start of the exclusion window, I employed the onset of the preseismic anomaly 5:05 UT for all the satellites (~40 minutes prior to the main shock). This time was obtained by Heki and Enomoto (2015) by searching significant positive bending in VTEC time series using AIC. As shown in Figure 13a, changing this starting time by ±12 minutes does not make significant differences in the reference curves for this pair of the satellite and the station.

Regarding the end time of the exclusion window, it is assumed that the postseismic drop (ionospheric hole) occurs by coseismic vertical crustal movement and hence over the ruptured fault. This will be confirmed later in Chapter 5 and supported by a numerical simulation, e.g. Figure 4a of Zettergren and Snively (2019). I determined the end time of the exclusion window by drawing the SIP trajectories to know the time for SIP to go out of the affected area (defined as the area above the fault with slips exceeding 3 m). Naturally, the end times depend on satellites (see Figure 11 inset maps). Table 1 lists the exclusion time windows for individual satellites used in this study (windows depend on regions of the stations, too, for some satellites).



669

670 **Figure 13.** The numerical experiments to move the starting (a) and ending (b) times of the
671 exclusion window in estimating the reference curves for the same data as in Figure 11a (station
672 3009, satellite 15). In (a), the starting time is set to 4:53, 4:59, 5:05 (nominal), 5:11, and 5:17 UT,
673 fixing the ending time to the nominal value (7:12UT). In (b) the ending time is set to 6:48, 7:00,
674 7:12 (nominal), 7:24, and 7:36 UT, fixing the starting time to the nominal value (5:05 UT). The
675 reference curve changes only slightly suggesting that the selection the excluding window is not a
676 crucial factor to calculate the VTEC anomalies for this case.

677

Table 1. List of the exclusion time windows, and the polynomial degrees optimized by the L-curve method for individual satellites used in this study. Some satellites have 2 values for the polynomial degrees[1,2] and the end of the exclusion windows[3,4], applied for 2 different areas in Japan.

GPS satellite number	Degree of polynomial	Start of the exclusion window (UT)	End of the exclusion window (UT)
5	4	5:05 (common)	5:54
9	5[1] and 7[2]		6:30
15	2[1] and 4[2]		7:12
18	3		6:00
21	5		6:00
26	4		6:06[3]and 6:25[4]
27	5[1] and 2[2]		6:48
28	5		5:48

[1]for northern Hokkaido (north of 43.5N), [2]for other parts, [3]for stations east of 139.5E, [4]for stations west of 139.5E

It should be noted that this study does not rely on the decay of the hole, which may last for hours, but avoid the spatial overlap of the hole with the LoS. This procedure enables us to isolate the VTEC anomalies caused by the earthquake robustly to a certain extent. Using the Figure 11a case, Figure 13b demonstrates that moving the ending time of the exclusion window by 24 minutes backward and forward let positive anomalies immediately before the earthquake change by only -3.7% and +10.8%, respectively. This suggests that the uncertainty in the ending time of a few tens of minutes is not crucial in isolating the preseismic VTEC anomalies.

For the satellites whose SIP does not go over the focal area (e.g. Sat. 18), I fixed the end of the excluding window at 10 minutes after the earthquake. For a few satellites (e.g. Sat.5 and Sat.28) with short postseismic VTEC data, I had to set up earlier end times for a part of stations (e.g. 5 minutes after the earthquake). I did not set up a specific elevation cut-off angle and assumed a thin layer at 300 km for STEC-VTEC conversion regardless of the elevations.

As for the point (3), the L-curve method is used to determine the optimum degree of polynomials curve (see Figure 7 of He and Heki, 2017). Root-mean-squares (rms) is calculated using the post-fit residuals outside the exclusion windows. Their dependences on the polynomial degree are shown in the left insets of Figure 11. The lower-left edge of the L-curve is considered to provide the most appropriate degree of polynomial to fit the VTEC changes. Table 1 also shows the degrees of polynomials for different satellites employed here. In Figure 11, the total time span of 5 hours is used for satellites 15 and 26 (the time spans are shorter for other satellites). The time spans also influence the best polynomial degree, i.e. the best degree tends to be higher for a longer time span. However, the shapes of the anomalies within the exclusion windows are not much influenced by the total time spans.

The departure from these reference curves (TEC anomalies) is used as the input for the 3D tomography calculation. In doing so, the VTEC anomalies were converted back to the STEC anomalies by dividing with cosine of the incidence angle of LoS to the 300 km layer. In short, I took advantage of VTEC for its simplicity in fitting the reference curves (because the apparent changes caused by elevation angle variations are already removed). However, the values after converting to STEC anomalies are used for 3D tomography.

As emphasized in Heki and Enomoto (2013) and He and Heki (2016), preseismic TEC anomalies take either positive or negative values. In Figure 11, I show examples of VTEC time-series showing positive and negative preseismic TEC anomalies with red and cyan curves, respectively. The difference would originate from the difference of the parts in ionosphere these LoS penetrate, i.e. the former would have penetrated more positive parts than negative parts of the electron density anomalies, and vice versa. The explanation on the variety of waveform of VTEC in penetrated LoS will be discussed in Chapter 5.

3.3 Resolution tests

For the 2011 Tohoku-oki earthquake case, ~6,800 blocks are set up over the Japanese Islands, the Sea of Japan, and the Korean Peninsula, with the size of 1.0^{o} (east-west) x 0.9^{o} (north-south) x 60 km (vertical) for altitudes 90-870 km (Figure 10). Now the dataset (VTEC residual) is ready, and the 3D tomography inversion could be performed to map the ionospheric electron density anomalies before the earthquake using the method explained in Chapter 2. However, it is often preferable to test the performance of the program and the resolution achieved by the available data set beforehand, by applying the program to synthetic data. Such a test is important to discuss

if the block size is appropriate. It is also important to know in which region the inversion results have enough resolution. This depends on spatial distribution of available LoS, i.e., it is essential that multiple LoS penetrate certain areas to infer the electron density anomalies there.

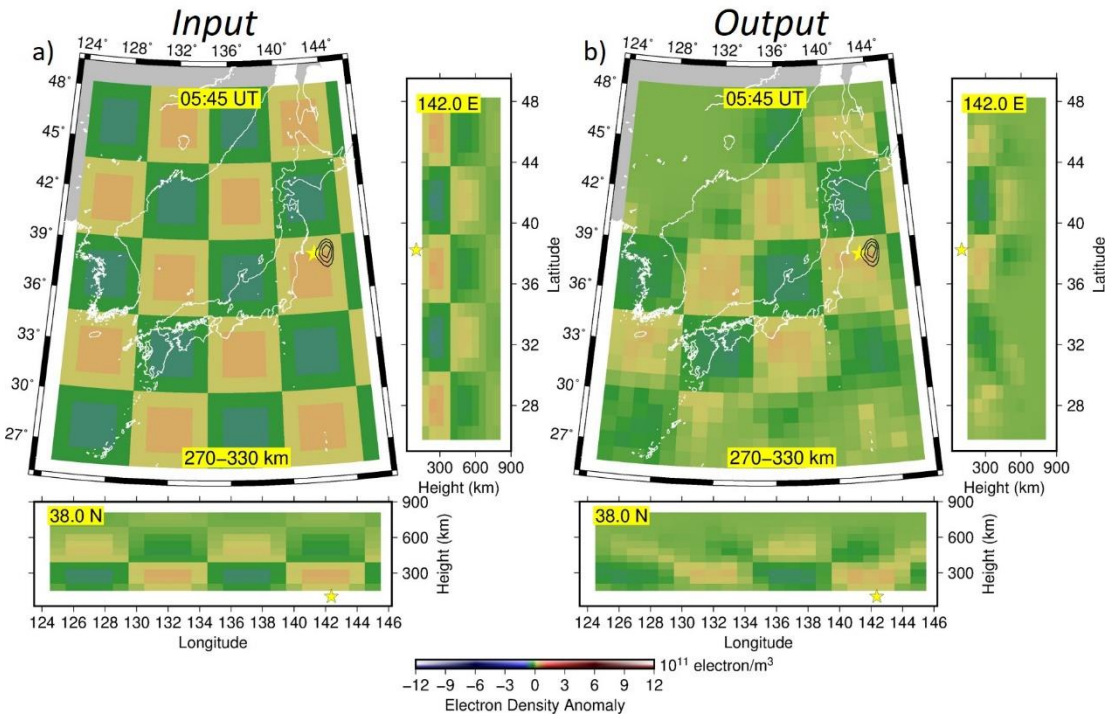


Figure 14. The resolution test with the classical checkerboard pattern. The assumed electron density anomalies (a) and the output of the 3D tomography (b) are given in map view and north-south, east-west profiles.

The accuracy of the 3D tomography can be assessed by performing the 3D tomographic inversion to recover artificial distribution of electron density anomalies using synthetic data. I first perform a test using the classical checkerboard pattern. I assumed the same satellite and station geometry as the epoch 05:45 UT on 2011 March 11, 1 minute before the Tohoku-oki earthquake,

752 to synthesize the input STEC data for the 3D tomography. In recovering the 3D distribution of
753 electron density anomalies, I applied the constraints explained in the previous chapter.

754 Figure 14a shows the assumed checkerboard pattern. It is composed of the electron density
755 anomalies of $\pm 2.00 \times 10^{11}$ el/m^3. I let the anomaly change gradually between the positive and
756 negative parts to make the pattern consistent with the continuity constraint. I also assumed the
757 amplitudes of the anomalies to decay in very high and low altitude to make it compatible with the
758 constraint around zero with altitude-dependent tolerances, assumed proportional to the a-priori
759 electron density profile predicted by the Chapman distribution.

760 Figure 14b shows the recovered pattern for the blocks at the altitude range 270-330 km.
761 The pattern is well recovered particularly over the land (i.e. the Japanese Islands) and the offshore
762 area within ~200 km from the coast, including the area above the rupture. Similarly, in the vertical
763 section the resolution remains good in the altitudes 150-510 km, although the amplitudes of the
764 recovered anomalies are ~2/3 of the input model possibly originating from the constraint around
765 zero. On the other hand, resolution is poor where we do not have enough LoS penetrations (Figures
766 10b and Figure 15). Such regions include the Pacific Ocean to the south of the rupture and the
767 region above North Korea and Russia. The checkerboard-test generally shows a high performance
768 of our 3D tomography in the region of interest. As suggested by Figure 15, vertical resolution is
769 poor even above NE Japan for the highest layers of the blocks.

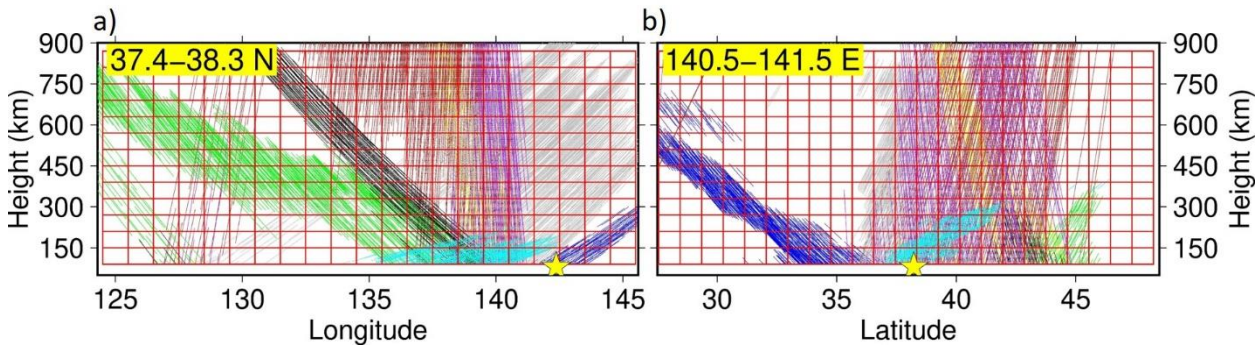
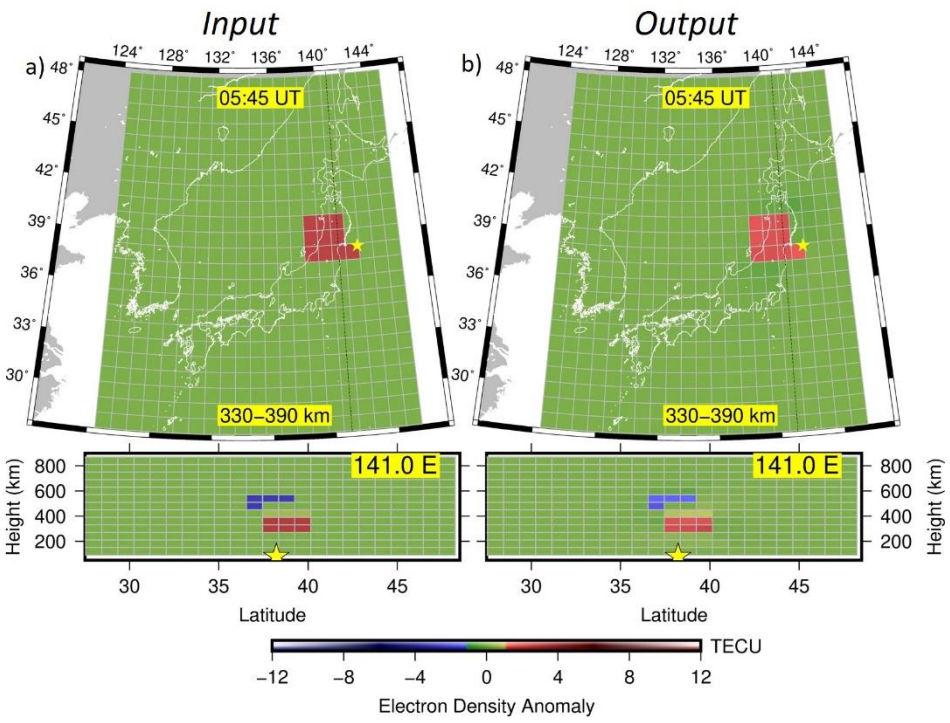


Figure 15. Vertical walls running east-west (a) and north-south (b) are assumed with the thickness of one block, and the LoS penetrating those walls are plotted with lines with colours corresponding to satellites (same colour as in Figure 10b, except for satellite 28 whose colour was changed into cyan for visual clarity). Electron density anomalies of voxels penetrated by many LoS with different angles are easier to be estimated than those penetrated by small number of LoS with similar directions.

I next assessed the robustness of our result for later discussions on preseismic electron density anomalies, by recovering patterns composed of a pair of positive and negative (±3.00 x 10^{11} el/m^3) anomalies in low and high altitudes, respectively, in neutral background (Figure 16a). The results (Figure 16b) well reproduced the assumed pattern of the positive anomaly again reduced to ~2/3 amplitude of the input model due to the constraints. Similarly, the positive and negative anomaly patterns in the latitudinal profiles are well recovered with only weak smears in surrounding blocks not exceeding a few percent of the assumed anomaly. The results of the two resolution tests show that our 3D tomography results are accurate enough in the region of interest, where the TEC anomalies appeared immediately before and after the 2011 Tohoku-oki earthquake.



787

788 **Figure 16.** Second resolution test for a pair of compact positive and negative anomalies above NE
789 Japan. The upper and bottom panels are horizontal view and latitudinal profile of the anomalies of
790 the assumed pattern (a) and the output of the 3D tomography (b).

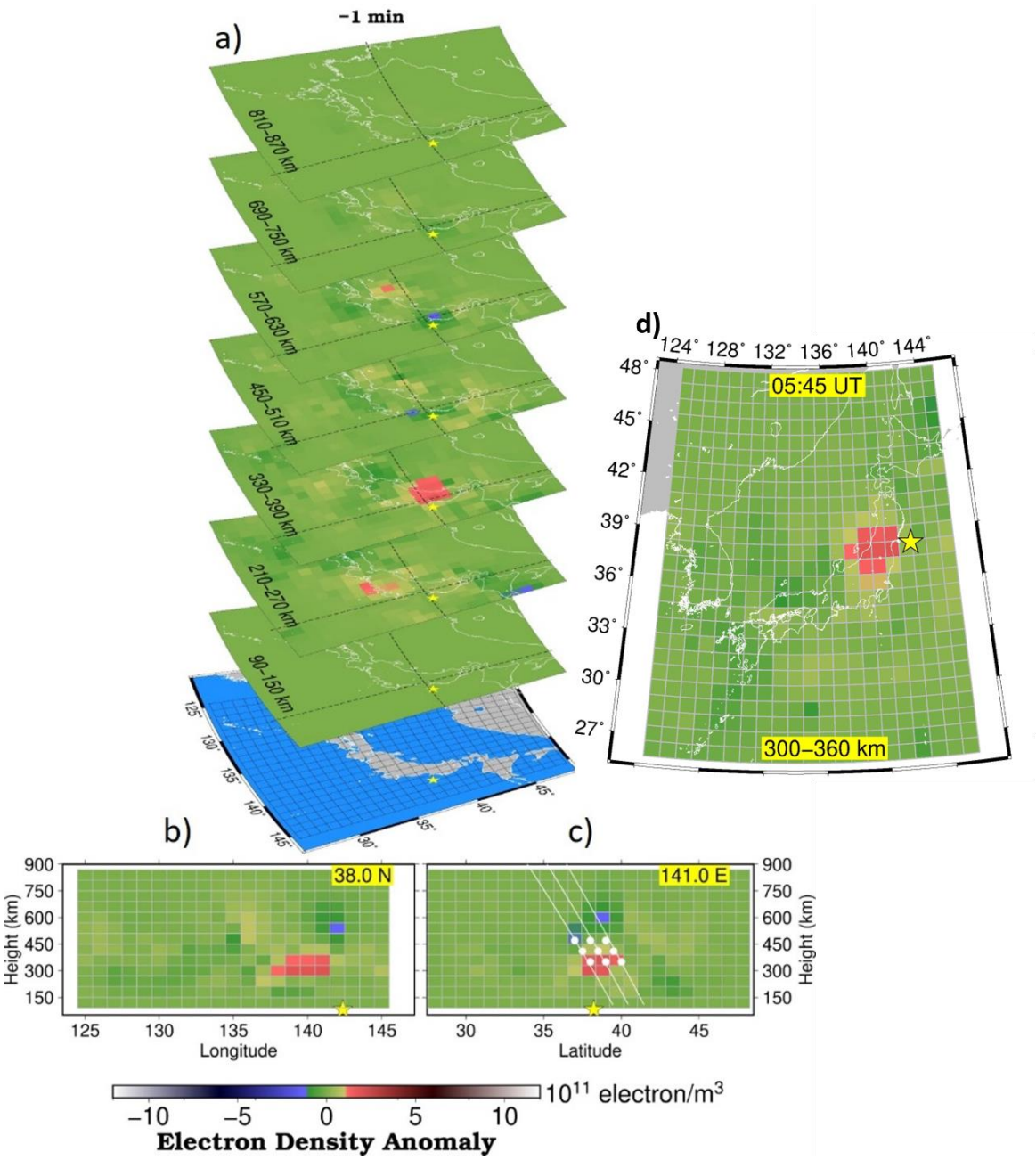
791

792 **3.4 Tomography results**

793 Figure 17a shows the map view of the 3D tomography result for altitudes of 90-870 km at
794 05:45 UT, 1 minute before the 2011 Tohoku-oki earthquake, with longitudinal and latitudinal
795 profiles. In Figure 18 I show the results at five epochs before the earthquake (40, 30, 20, 10, and
796 1 minute before the earthquake). I confirmed beforehand by resolution tests that the performance
797 of the tomography remains high for all these epochs. The results present that the strong positive
798 electron density anomalies occurred at 270-330 km and 330-390 km altitude layers and the
799 anomalies grow large without notable pattern change or spatial drifts toward the main shock. In

800 fact, the latitude of the voxel showing the largest positive anomaly stays around 38°N during the
801 40 minutes period.

802



803

804 **Figure 17.** 3D tomography results of electron density anomalies 1 minute before the Tohoku-oki
805 earthquake (a). The east-west and north-south profiles are also shown in (b) and (c), respectively.
806 The white lines in (c) show the geomagnetic fields, and yellow stars show the latitude and
807 longitude of the epicenter. White circles in (c) show selected positions used to draw Figure 22.
808 The results for other epochs are given in Figure 18. An enlarged plan view showing positive
809 electron density anomaly is given in (d).

An important feature is that the positive anomaly lies above the land of NE Japan rather than right above the focal area (Figure 17d). Its implication will be discussed later. The longitudinal and latitudinal profiles (Figure 17b, c) show that the positive anomaly is the strongest at altitude 270-390 km. Above this positive anomaly lies the negative anomaly at altitude ~600 km. These two anomalies are diffuse, and it is not very clear if they lie along the geomagnetic field. Nevertheless, the pattern resembles to the earlier report for the 3D structure of the preseismic anomalies of the 2015 Illapel earthquake (He and Heki, 2018), a pair of positive (height 150-225 km) and negative (height 450-525 km) anomalies located along the geomagnetic field.

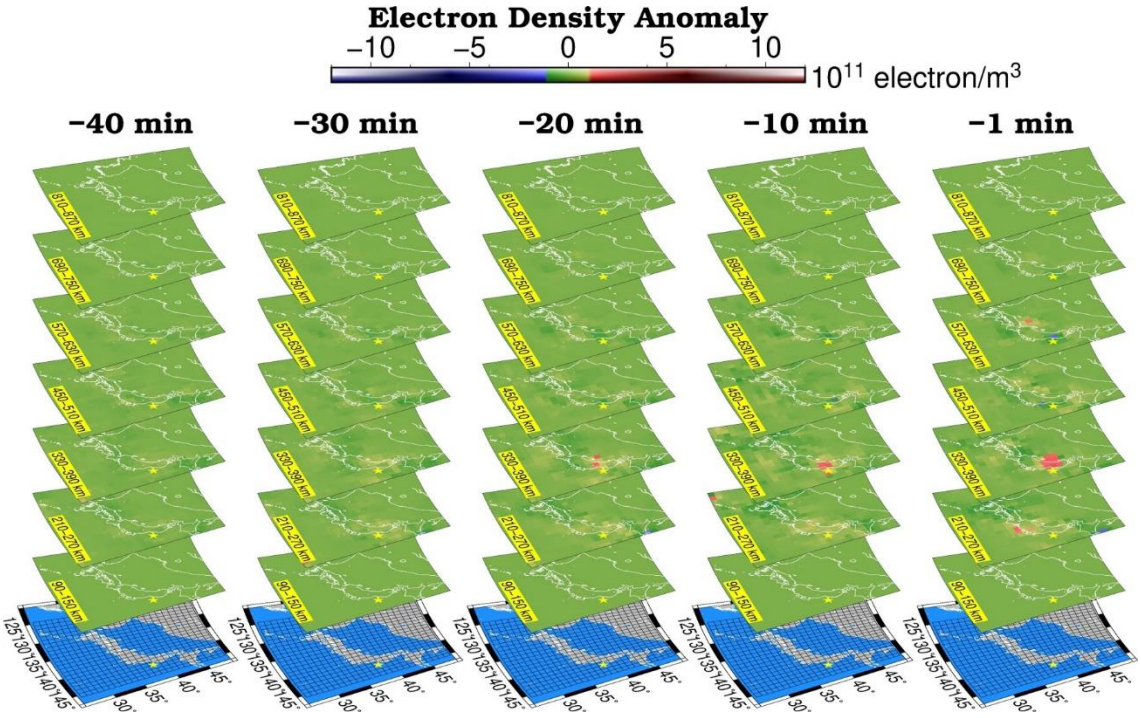
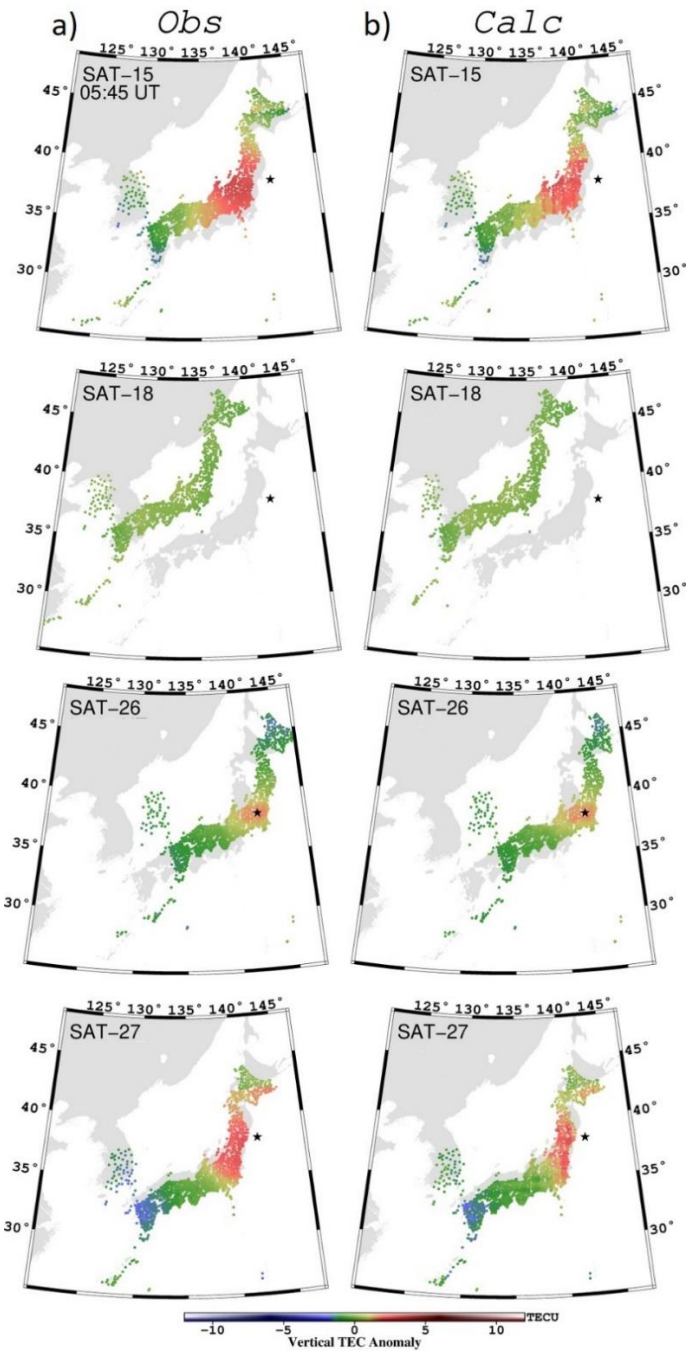


Figure 18. 3D tomography results of electron density anomalies for altitudes 90-870 km at five epochs, 40, 30, 20, 10, and 1 minute before the 2011 Tohoku-oki earthquake.

822 Figure 19 compares the observed and calculated anomalies for four satellites, 15, 18, 26,
823 and 27, at the epoch 1 minute before the main shock. The “observed” anomalies (Figure 19a) are
824 those obtained as the departure from the reference curves to VTEC time series, and they are plotted
825 at their SIP. On the other hand, the “calculated” anomalies (Figure 19b) were derived as the sum
826 of the products of the estimated electron density anomalies (Figure 17) and the penetration lengths
827 of voxels along the LoS. Such calculated STEC anomalies are converted to VTEC for comparison
828 with the observed anomalies. These two are expected to nearly coincide if the 3D tomography
829 inversion is successful. We can see that the observed TEC anomalies are well reproduced by the
830 estimated 3D electron density anomalies shown in Figure 17.



831

832 **Figure 19.** Comparison of the observed (a) and calculated (b) VTEC anomalies for 4 GPS satellites
833 at the epoch at 05:45 UT, 1 minute before the earthquake. They are mostly consistent with each
834 other showing that the estimated 3D electron density anomaly structure well explains the observed
835 TEC changes.

836 Next, I perform two additional assessments of the accuracy; (1) confirming the reduction
837 of the variances of the original STEC anomalies to those of the post-fit residuals (the difference
838 between the calculated and the observed values compared in Fig.19), and (2) checking the
839 consistency of the subset data not used for 3D tomography with the result of the 3D tomography
840 estimated using the rest of the data. Figure 20a shows the results of (1) for three different time
841 epochs. Original STEC residuals have large variance around zero, but the post-fit STEC residuals
842 of the 3D tomography show much reduced scatter around zero. Together with Figure 19, this would
843 imply that the estimated 3D distribution of the electron density anomalies well explains the
844 observed STEC.

845 Figure 20b shows the result of a validation test for the epoch 05:45 UT. I removed
846 randomly selected 10% of the original input data as the validation data subset. Next, I used the
847 remaining 90% as the input to our 3D tomography method. Then, I calculated the STEC for the
848 removed 10% subset using the estimated 3D electron density anomaly distribution. They are
849 expected to coincide with each other. Figure 20b shows that the coincidence is as good as ~0.51
850 TECU.

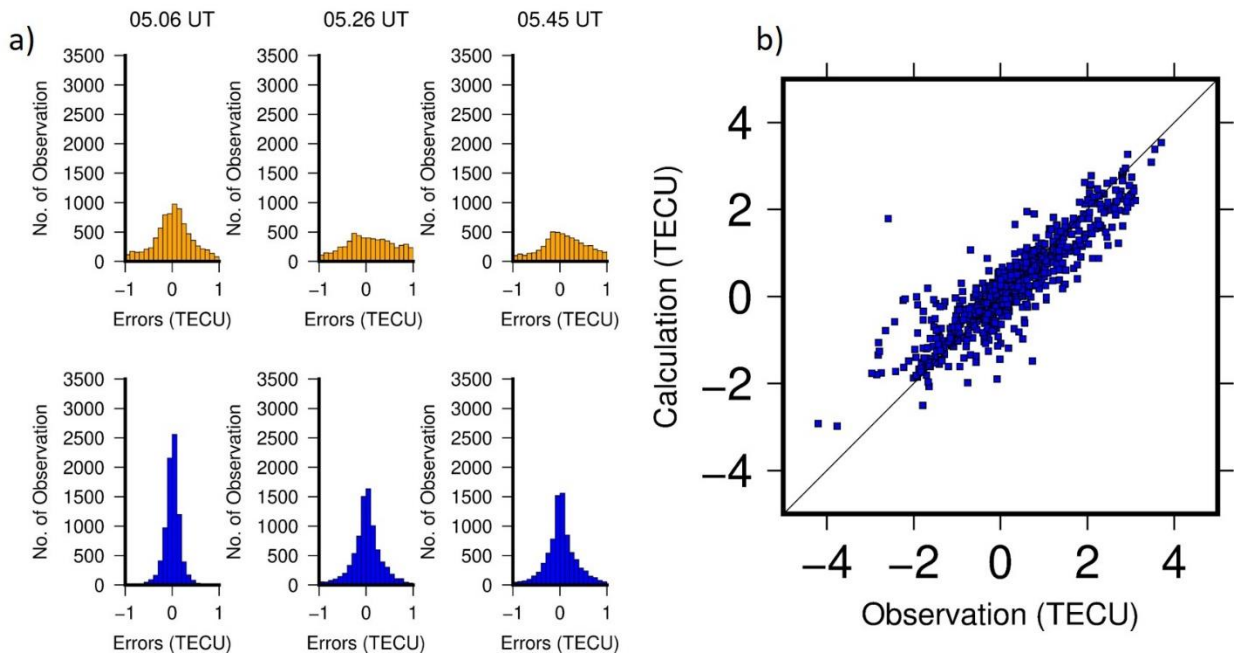


Figure 20. (a) The histograms of the STEC input to the 3D tomography (upper panel in orange), and the post-fit residuals (lower panel in blue) at three-time epochs (40 minutes, 20 minutes, and 1 minute before earthquake). (b) Comparison between the randomly removed 10% subset of the observed STEC data at 05:45 UT (horizontal axis) and those calculated using the 3D electron density anomalies estimated with the remaining 90% data (vertical axis). The rms of the scatter around the 45 degrees line is ~0. 51 TECU.

Figure 21 compares the tomography results based on three different settings of the constraint around zero, i.e., 1, 3, 10% of the Chapman distribution. It can be seen that the positive anomaly ~300 km high and negative anomaly ~600 km high persistently appear for those solutions. At the same time, a weaker constraint tends to yield complicated patterns in layers near the top of the blocks.

In Figure 15, I showed the distribution of the LoS connecting ground GNSS stations and the GPS satellites penetrating the vertical walls running east-west (a) and north-south (b) with the

one-block thickness. We can see that blocks with altitude up to 600 km above NE Japan are penetrated by many LoS with multiple satellites having different penetration angles. On the other hand, the highest layers are penetrated only by nearly vertical LoS, suggesting difficulty in constraining altitudes of electron density anomalies there. I think that such irregular anomalies emerging in the highest layers for weak constraint cases are not real.

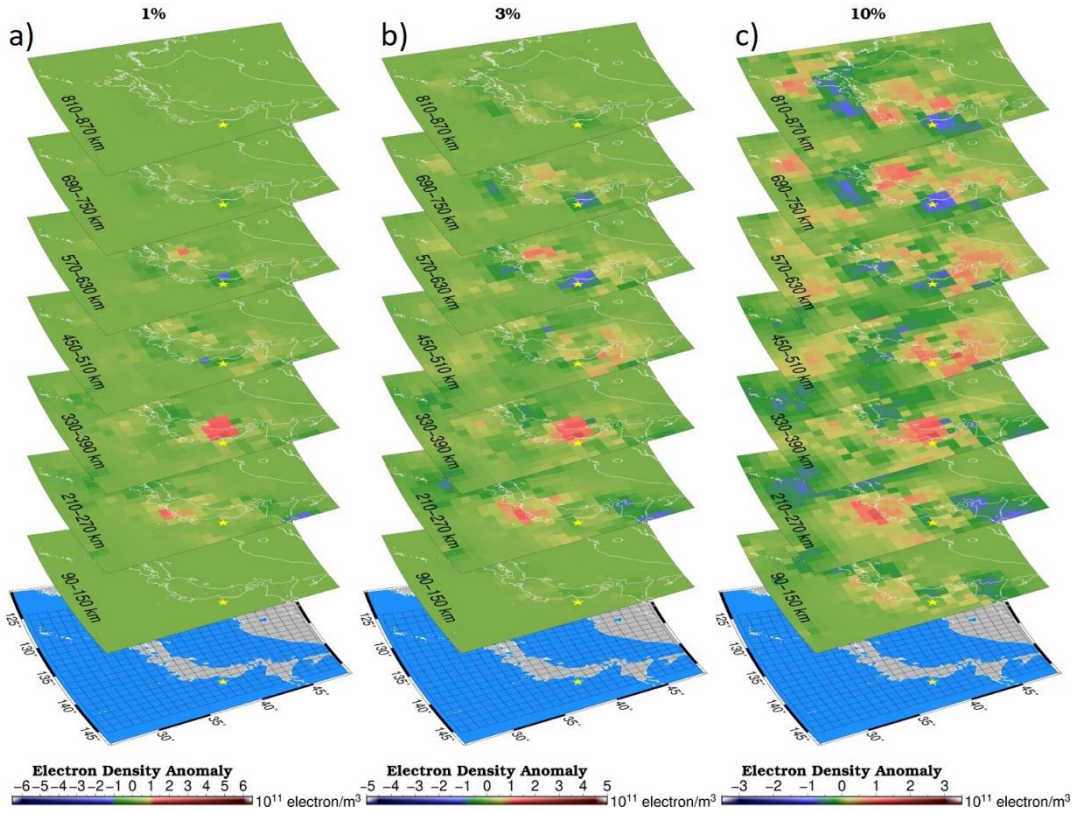


Figure 21. 3D tomography results of electron density anomalies at the epoch 1 minute before the mainshock with different strength of constraints around zero, i.e. 1 % (a), 3 % (b), and 10 % (c) of the Chapman distribution of the electron density.

3.5 Growth and polarity balances of the preseismic anomalies

To further study the evolution of the electron density anomalies immediately before the earthquake, in Figure 22a, I plot the electron density anomalies at points with three different altitudes, 330-390 km, 390-450 km, and 450-510 km (white circles in Figure 17c) connected with the geomagnetic field. The three altitudes correspond to the center of positive anomaly, middle point between the positive and negative anomalies, and the center of negative anomaly, respectively.

Figure 22a shows the averages of three blocks at low, medium, and high altitudes every 3 minutes before and after the earthquake. The positive anomalies show larger values than negative anomalies. However, this does not necessarily mean the dominance of the spatially integrated positive anomalies. Figure 22b indicates the total amount of positive and negative electron density anomalies obtained by integrating them in space. They are well balanced, suggesting that the growth of the anomalies occurred as the electron transport rather than net increase or decrease of electrons.

The build-up of the positive and negative anomalies starts ~40 minutes before the earthquake. They grow until ~20 minutes before the main shock and remain nearly constant until the earthquake. After the earthquake, the anomalies remain stationary for ~10 minutes and start to decay. I have no idea on the fluctuations of the curve around 5.4-5.6 UT and sudden increase of the negative anomaly after 5.6 UT in Figure 22b. They may reflect a certain instability coming from the VTEC observation errors. It should be noted that I did not perform in our tomography any temporal smoothing which would be an effective remedy to reduce such instability.

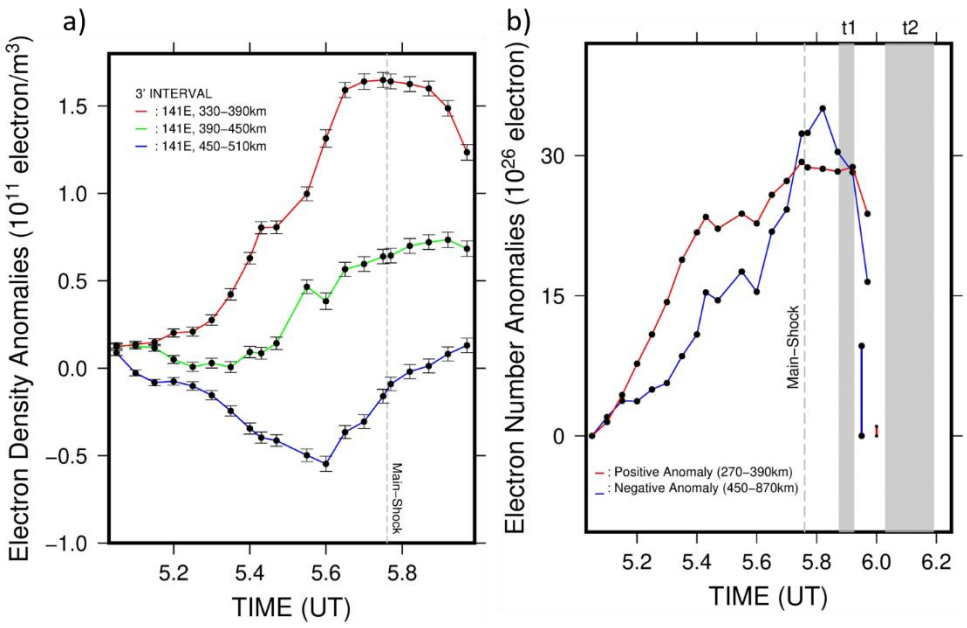


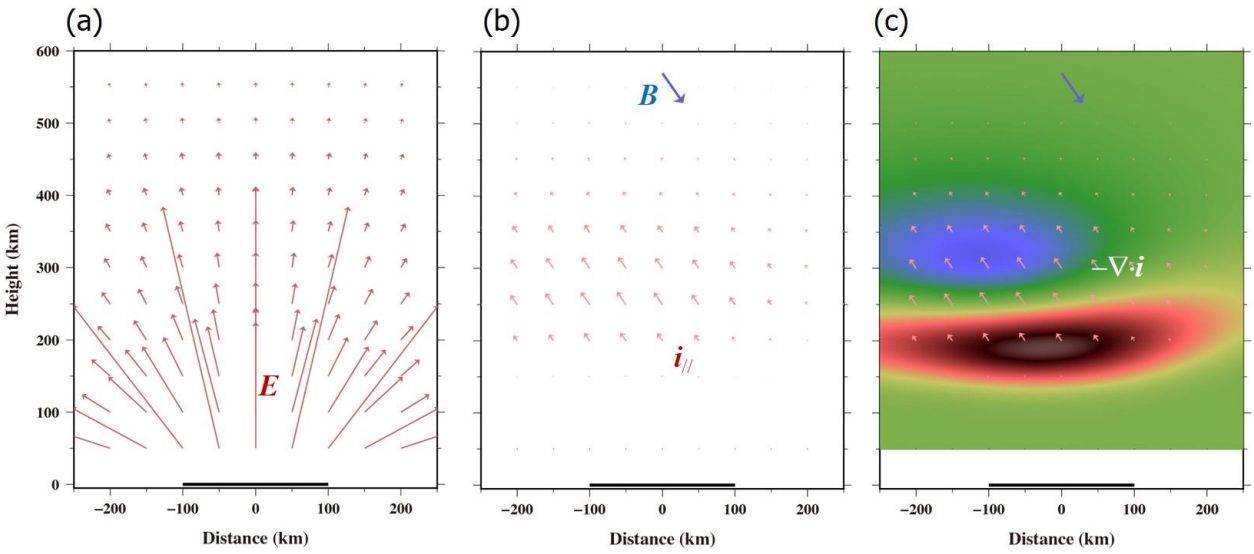
Figure 22. (a) The evolution of the average estimated electron density anomalies of the three different blocks at the 3 altitudes, 360 km, 420 km, 480 km (see Fig.17c for positions), with 3-minutes interval. The error bars are the average of the formal errors of the 3 voxels sampled at the 3 altitudes. (b) shows the integrated amount of positive and negative anomalies at lower (270-390 km) and higher (450-870 km) altitude voxels, respectively. To the right side of (b), I show the spatially integrated increase in negative (blue) and positive (red) postseismic electron density anomalies measured as the difference between the two periods shown in grey squares (see Figure 34 in Chapter 5).

3.6 Discussion on the physical mechanism of the preseismic anomalies

The result showed that the total amounts of the positive and negative electron density anomalies increased in a similar manner (Figure 22b) suggesting little changes in the total number of electrons in the preseismic stage. Hence, such changes would have occurred without net increase or decrease of electrons, e.g., by electron transportation, rather than enhanced ionization (generation of new free electrons) or recombination (loss of free electrons).

Another important fact is that the strong positive anomalies before the 2011 earthquake emerge only above land (Figure 17d). This suggests that the electron redistribution is due to electric fields made by surface electric charges. Such surface charges would be relatively stable on land, but they diffuse rapidly in the ocean due to high electric conductivity of sea water (areal density of the surface charges would be determined by the balance between the production at depth and the diffusion at the surface). Considering these features, I discuss possible physical mechanisms connecting the surface electric charges to the preseismic ionospheric electron redistributions.

Two hypotheses have been proposed before to explain how surface electric charges redistribute ionospheric electrons. Kuo et al. (2014) showed that the anomaly can be generated by an upward electric current from stressed rock. This leads to the westward Hall electric field $\boldsymbol{E}$. This $\boldsymbol{E}$, together with the geomagnetic field $\boldsymbol{B}$, drives downward $\boldsymbol{E}\times\boldsymbol{B}$ drift of the ionospheric plasma and makes a pair of positive and negative electron density anomalies. This model, however, needs large electric fields near ground to let substantial electric current flow through the highly resistive lower atmosphere. Kelley et al. (2017) proposed that the $\boldsymbol{E}\times\boldsymbol{B}$ drift could be driven directly by electric fields made by surface electric charges. Their model needs the surface electric fields only ~1/500 of the fair-weather field to produce the anomalies observed before the 2011 Tohoku-oki earthquake.



931

932 **Figure 23.** A two-dimensional image of the preseismic electron redistribution by surface electric
933 charges. (a) Positive charges distributed on the surface (grey line at the bottom) make upward
934 electric field ***E***, and (b) the component parallel with the geomagnetic field ***B*** exerts electromotive
935 forces and drives electric current $\boldsymbol{i}_{//}$ along the geomagnetic field where there are enough free
936 electrons. (c) Convergence and divergence of the electron flow makes positive (red) and negative
937 (blue) electron density anomalies, respectively. This is a qualitative model, and scales to convert
938 the illustrated quantities to real values are not given.

939

940 Muafiry and Heki (2020) proposed a new model focusing on the induced polarization, that
941 would occur together with the process proposed by Kelley et al. (2017). Figure 23 qualitatively
942 illustrates the idea. Electric fields ***E*** made by surface charges would reach the ionosphere (Figure
943 23a). The field generates electromotive forces and makes electrons move along geomagnetic
944 fields. If surface charges are positive, electron movements will be downward, and the current will
945 be upward ($\boldsymbol{i}_{//}$ in Figure 23b). The current will continue until the induced electric field cancels the
946 external field made by surface charges, making the electric potential uniform along the magnetic
947 field. The current will depend on the along-***B*** component of the external electric field and the
948 density of free electrons as a function of altitude. The non-uniform electric currents would result

in convergence/divergence of electrons and make positive/negative electron density anomalies at the lower/higher ionosphere along the magnetic field (Figure 23c), the structure found in Chile (He and Heki, 2018) and in Japan (this thesis) by the 3D tomography.

The model is qualitative, and it is not supposed to give actual figures for quantities such as areal density of surface charges and $\boldsymbol{E}$. This stems from the limitation of the GNSS-TEC method, i.e., GNSS can sense only electrons and cannot count positive ions. In fact, substantial amount of positive ion would move together with electrons to keep the plasma "nearly" neutral (there should be deviation from neutral, however, to cancel the external electric fields by the induced fields). In short, the 3D tomography results do not allow us to directly infer $\boldsymbol{E}$ or $\boldsymbol{i}_{//}$.

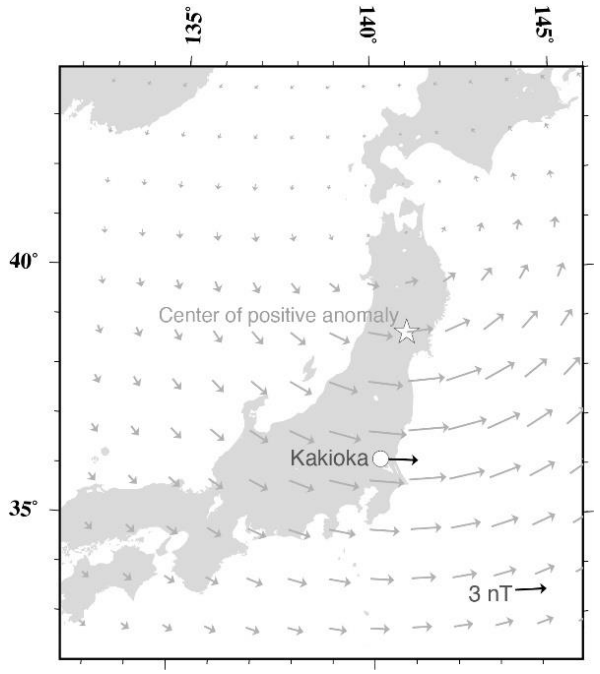


Figure 24. Magnetic field on the surface caused by the upward current along geomagnetic field above the star (the center of the positive anomaly), equivalent to cause ~0.15 of electron transport given in Figure 7b from altitude 330 km to 600 km. This makes disturbing field of ~3 nT eastward at the Kakioka station, consistent with those reported in Heki and Enomoto (2013).

One external test of the model might come from the magnetic fields possibly generated by the upward current along B ($\boldsymbol{i}_{//}$ in Figure 23b). Such a current would make eastward magnetic fields on surface, mainly in the region to the south of the epicenter (Figure 24). As discussed above, the electron density anomalies as revealed by 3D tomography (Figures 17) only reflect the electron redistribution, and the net current would depend on the movements of positive ions. I drew Figure 24 assuming an arbitrary current, to let 4.5 x 10^{26} electrons (~0.15 of the amount in Figure 22b) flow along a thin line extending from the center of positive electron density anomaly at 330 km altitude upward along the magnetic field to 600 km altitude in 40 minutes. Then the Bio-Savard's law predicts the eastward field of ~3 nT in the Kanto District (Figure 24). This nearly coincides with the change in declination observed at the Kakioka observatory in Kanto (relative to Kanoya in Kyushu) starting ~40 minutes before the earthquake as reported in Figure 4 of Heki and Enomoto (2013). Anyway, the assumption is arbitrary (the value 0.15 does not have a theoretical basis), and Figures 23 and 24 just provide a rough sketch illustrating how the induced polarization occurs.

It is also assumed that the declination change at Kakioka (Heki and Enomoto, 2013) was not a regular space weather phenomenon. It should be born in mind, however, that the 2011 Tohoku-oki earthquake occurred during a magnetic storm. So, a careful study is needed to attribute the observed declination changes to the ionospheric electron redistribution process as proposed in this study. It would be also important to detect magnetic field changes immediately before many other large earthquakes to draw a more realistic picture of the whole process.

Chapter 4: 3D Tomography of the Ionospheric Anomalies Before the 2010 Maule Earthquake, Chile: Comparison with the 2011 Tohoku-oki and 2015 Illapel Earthquake

4.1 Introduction: Structure of preseismic ionospheric anomalies

In this chapter, the short-term presesimic ionospheric anomalies before the 2011 Tohoku-oki earthquake is compare with other earthquakes for the sake of better understanding of their features. So far, we studied examples of the 3D distributions of ionospheric electron density anomalies immediately before two large earthquakes, i.e. 2011 Tohoku-oki (M_w9.0, this thesis) and 2015 Illapel earthquake, central Chile (M_w8.3, He and Heki, 2018). Both cases show a common structure, lower positive and higher negative electron density anomalies. Their vertical profiles suggest that the altitudes of the positive and negative anomalies before the 2011 earthquake (~300 and ~600 km) are somewhat higher than those of the 2015 earthquake (~200 and ~500 km).

On the other hand, horizontal extents of anomalies are little different in the two cases, i.e. the positive anomalies of 2011 lie within circles with diameter of ~300 km above the land region and not above the epicenter (off-shore). This strongly supports the physical model presented in the previous chapter that electric charges on the land surface redistributed ionospheric electrons. Regarding the 2015 Illapel earthquake, its epicenter is close to the coast, and such a feature, e.g. lack of the anomaly above the ocean, is not clear.

In this chapter, I analyze the 3D structure of the preseismic ionospheric anomaly of the 2010 M_w 8.8 Maule earthquake, another M9-class earthquake occurred in central Chile ~1 year before the 2011 Tohoku-oki earthquake. I follow the same 3D tomography approach employed in He and Heki (2018) and this thesis.

4.2 Data set

In the morning (03:34 in local time) of 27 February 2010, a Mw8.8 earthquake ruptured the Topocalma, Carranza, and Arauco segments of the Chilean subduction zone (Jara-Munoz et al., 2015). The epicenter of this Maule earthquake is located at the geographic latitude of 35.9°S (geomagnetic latitude of 36.1°S), and He and Heki (2016) reported that the geomagnetic activity was low before and after this earthquake. Here I use the GNSS-TEC data extracted from raw RINEX data files obtained at 89 permanent GNSS stations in South America (Figure 25). The TEC data from six GPS satellites (11, 13, 17, 20, 23 and 32) are used. The spatial coverage of the GNSS stations is not so good as in the 2015 Illapel earthquake case (He and Heki, 2018) because many of the stations used there were not operating in 2010. The station density is much lower than the 2011 Tohoku-oki case (this thesis).

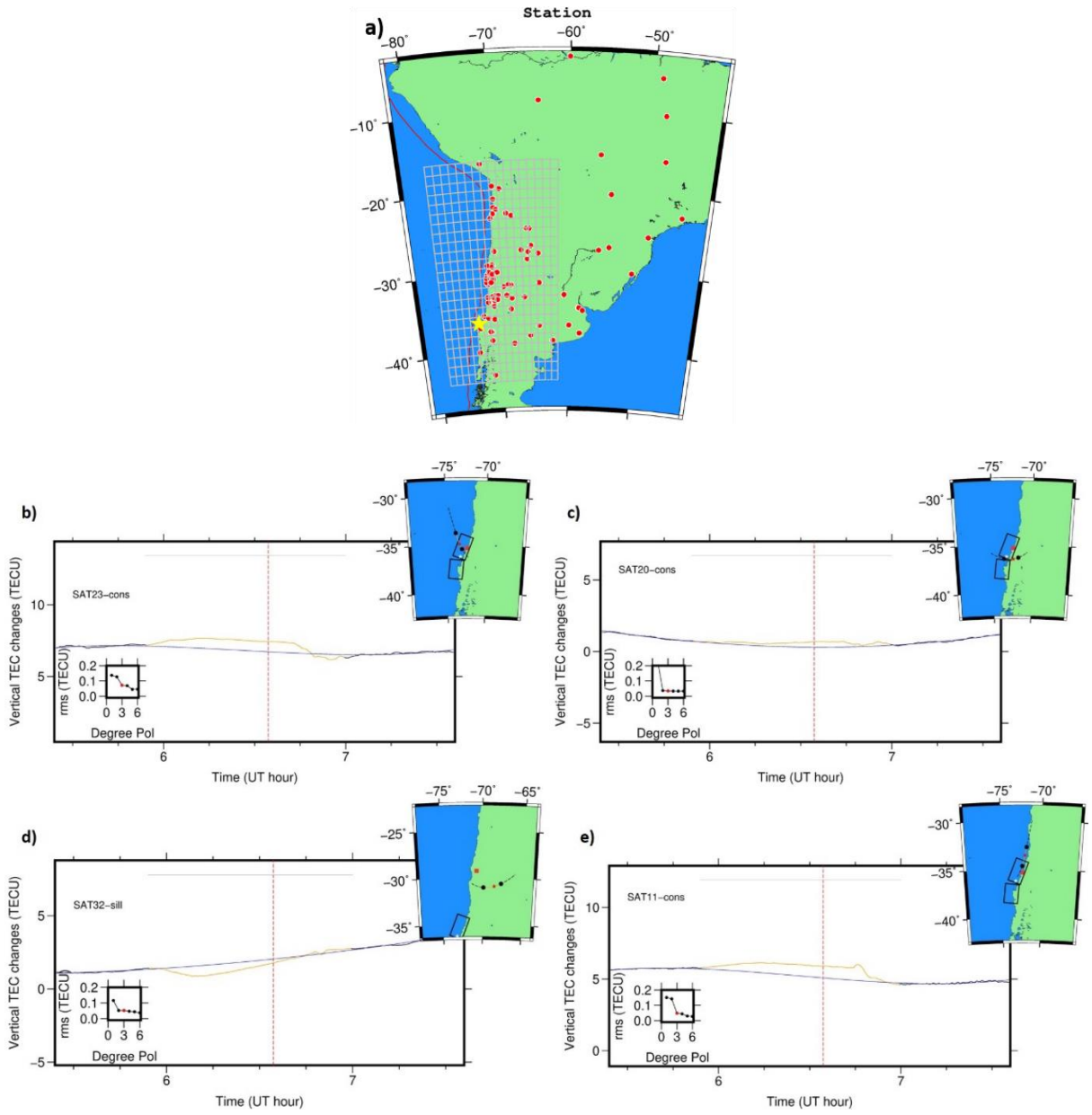


Figure 25. Maps showing the GNSS station distribution (red dots) and the voxels for 3D tomography above the middle South-America (a). Yellow star indicates the epicenter of the 2010 Maule (M_w8.8) Earthquake. A red curve illustrates the Peru-Chile Trench, the boundary between the Nazca and the South American Plates. Panels (b-e) show VTEC time series (yellow curves) and reference curves by best-fit polynomials (blue curves) for satellite-receiver pairs with four GPS satellites, i.e. Sat.23-CONS (b), Sat.20-CONS (c), Sat.32-SILL (d), and Sat.11-CONS (e). Insets of (b-e) show the behaviour of the residuals for the change of the polynomial degrees (L-curve method to optimize the degree). See the caption of Figure 11 for other symbols.

4.3 Data processing strategy

The 3D tomography input data are the STEC residuals (converted from VTEC) from available station-satellite pairs with LoS penetrating the voxels. I followed the procedure described in Chapter 3.3 of this thesis. I first calculate the absolute VTEC for each pair by multiplying the de-biased STEC with the cosine of the incidence angle of LoS into a thin shell at 300 km altitude from the surface. The inter-frequency biases (station and satellite biases) are removed beforehand. The satellite biases are extracted from the header of the Global Ionosphere Maps (GIM) downloaded from aiub.unibe.ch/CODE. The receiver biases were estimated so that the scatters of VTEC during the stable local time (from midnight to dawn) are minimized (minimum scalloping).

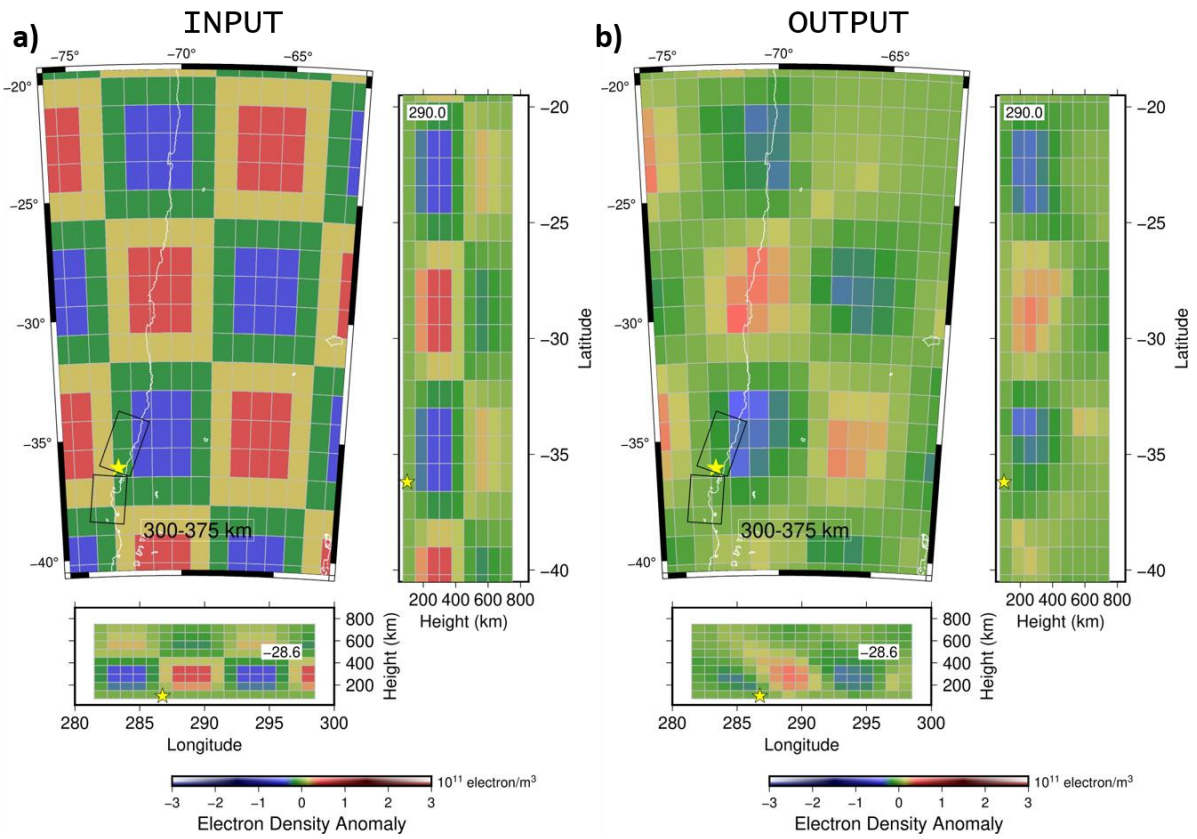
The VTEC anomaly is obtained as the difference between the observed VTEC and reference curves estimated as polynomials whose degree is optimized by the L-curve method (selection of best degree of polynomial). The exclusion time-window was used in estimating the reference curves. The window starts from 40 minutes before the main shock following the detection of the bending done in Heki and Enomoto (2015) using AIC. As for the end time of the exclusion window, I employed 07:00 UT when the SIP trajectories of GPS-23 and GPS-20 left the focal region (Figure 25b and 25c), i.e. the position of the expected postseismic ionospheric hole. For the remaining GPS satellites, I used the same settings because this window worked fine for those satellite, too. VTEC residuals were converted back to STEC residuals by dividing with the cosine of the incidence angle that were used to convert the de-biased STEC to VTEC.

4.4 Resolution test

I set up the voxels for the 3D tomography of the electron density anomalies before and after the 2010 Maule earthquake. The 792 blocks are distributed above South America, with the size of 1.0^{o} (east-west) x 1.2^{o} (north-south) x 75 km (vertical) for the altitude range 75-750 km (Figure 25).

The distribution of LoS and the block size are important factors for the accuracy of the tomography results. Before performing 3D tomography using the real STEC residual data, I first perform tests with synthetic data to recover artificial distribution of electron density anomalies to evaluate the accuracy of the method. I employ the classical checkerboard pattern for the resolution test. I assumed the same satellite and station geometry as the epoch 06:33 UT, 1 minute before the earthquake, to synthesize the input STEC data for the 3D tomography. In recovering the 3D distribution of electron density anomalies, I applied the same constraints as the 2011 Tohoku-oki case (continuity constraint and constraint around zero with altitude-dependent tolerance) as explained in the previous chapter.

Figure 26a shows the assumed checkerboard pattern. It is composed of the electron density anomalies of $\pm 2.00 \times 10^{11}$ el/m^3. I let the anomaly change gradually between the positive and negative parts to make the pattern consistent with the continuity constraint. I also assumed the amplitudes of the anomalies to decay in very high and low ionosphere to make it compatible with the other constraint.



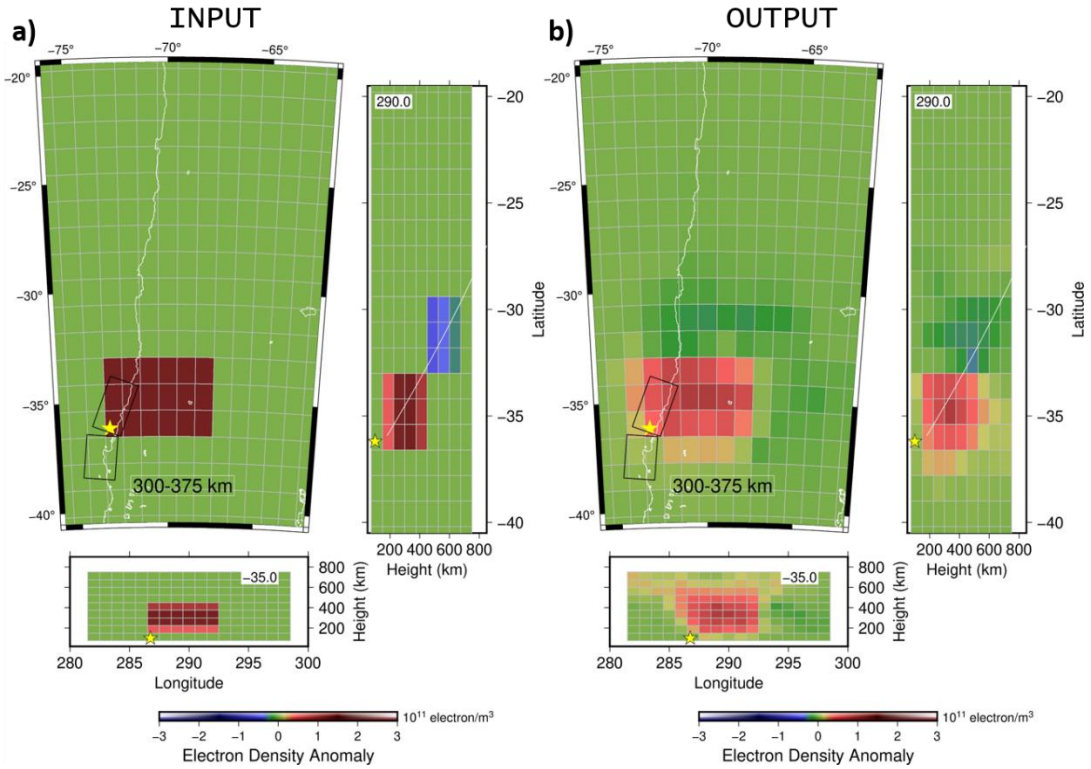
1068

1069 **Figure 26**. The resolution test of the 3D tomography of ionospheric electron density anomalies
1070 before the 2010 Maule earthquake, central Chile, with the classical checkerboard pattern. The
1071 assumed electron density anomalies (a) and the output of the 3D tomography (b) are given in map
1072 view and north-south, east-west profiles. The yellow stars indicate the position of the epicenter of
1073 the earthquake. Black rectangles is an approximate rupture area.

1074

1075 Figure 26b shows the recovered pattern for the blocks at the altitude range 300-375 km.
1076 The pattern is well recovered particularly over the land and the offshore area within ~100 km from
1077 the coast, including the area above the rupture. Similarly, in the vertical section the resolution
1078 remains good in the altitudes 150-525 km, although the amplitudes of the recovered anomalies are
1079 ~1/3 of the input model due possibly to the constraint around zero. On the other hand, resolution

1080 is poor where LoS do not penetrate the voxels (Figure 30). Such regions include the northeastern
1081 part of the studied area.



1082

1083 **Figure 27**. The second resolution test for a pair of positive and negative anomalies above middle
1084 of South America. The upper, bottom, and right panels are horizontal view, longitudinal and
1085 latitudinal profiles of the anomalies of the assumed pattern (a) and the output of the 3D tomography
1086 (b). Black rectangles is an approximate rupture area.

1087

1088 I next assessed the robustness of our result by recovering patterns composed of a pair of
1089 positive and negative ($\pm 2.30 \times 10^{11}$ el/m^3) anomalies in low and high altitudes along the
1090 geomagnetic field, respectively, in neutral background (Figure 27a). The results (Figure 27b) well
1091 reproduced the assumed pattern of the positive anomaly again reduced to ~2/3 amplitude of the
1092 input model due to the constraint.

However, the high-altitude negative anomaly pattern in the latitudinal profile is not well recovered. This indicates the limited availability of LoS is in the region where the negative anomaly is supposed to appear (Figure 30). The results of the two resolution tests show that our 3D tomography results are accurate enough in a part of the region of interest, i.e., where the positive TEC anomalies are expected to emerge immediately before the 2010 Maule earthquake. However, it would be difficult to identify the negative anomaly expected to emerge at a higher altitude.

4.5 Tomography result

Figure 28 shows the map view of the 3D tomography result for altitudes of 75-750km at 06:33 UT, 1 minute before the 2010 Maule earthquake, together with longitudinal and latitudinal profiles. Figure 29 shows the results at three epochs before the earthquake (40, 22 and 1 minutes before the earthquake). I confirmed beforehand that the performance of the tomography 40 and 22 minutes before earthquake remains comparable to that 1 minute before earthquake shown in Figures 26 and 27. The results present that the strong positive electron density anomalies occurred at the 225-375 km altitude layers and the anomalies grow large without notable pattern change or spatial drifts toward the main shock. In fact, the latitude of the voxel showing the largest positive anomaly stays around 28^{o}N during the 40 minutes period. The high-altitude negative electron density anomaly is not clear in this result. Figure 30 shows the LoS distributions in EW and NS profiles where the negative anomaly is supposed to appear. In comparison with Figure 15 for the 2011 Tohoku-oki earthquake, it can be seen that there are not enough number of paths penetrating

voxels in those areas. This is because the GNSS stations used here are fewer than the earlier study for the 2015 Illapel earthquake (station increased markedly after the 2010 earthquake), and they concentrate near the epicenter.

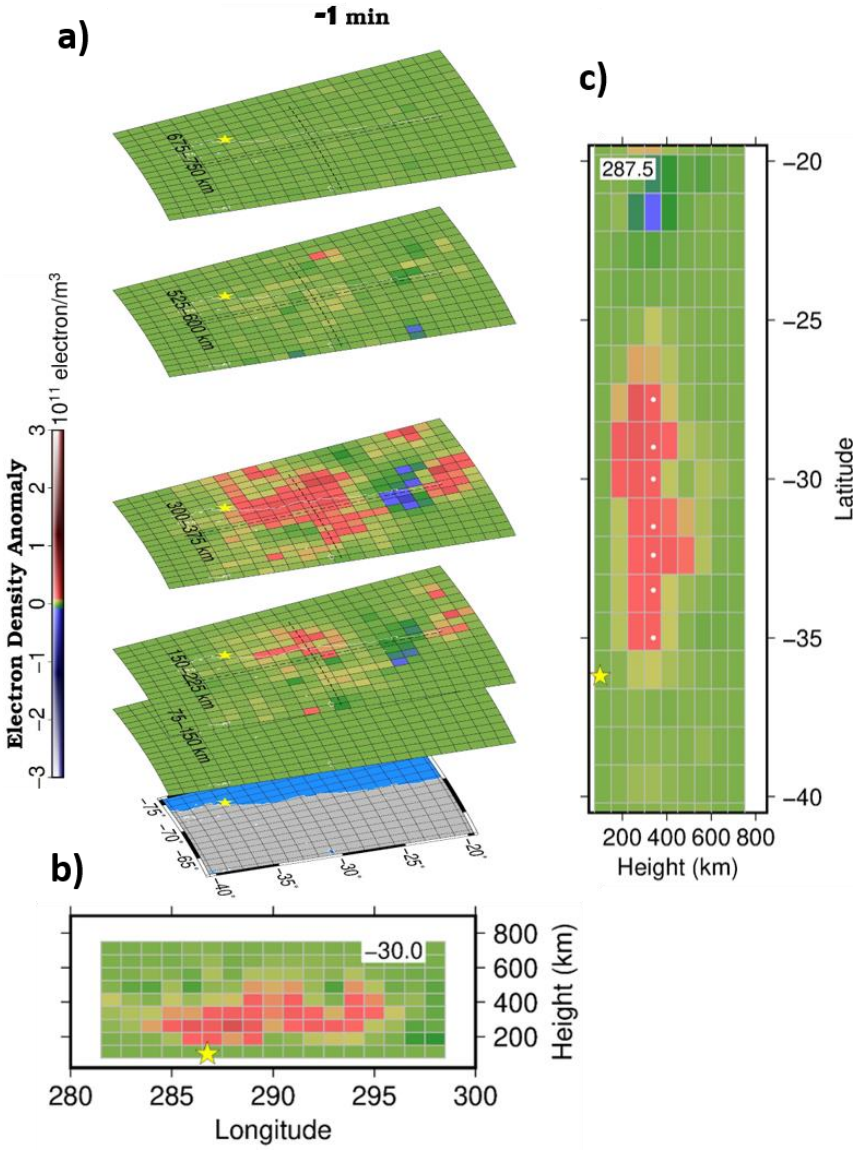
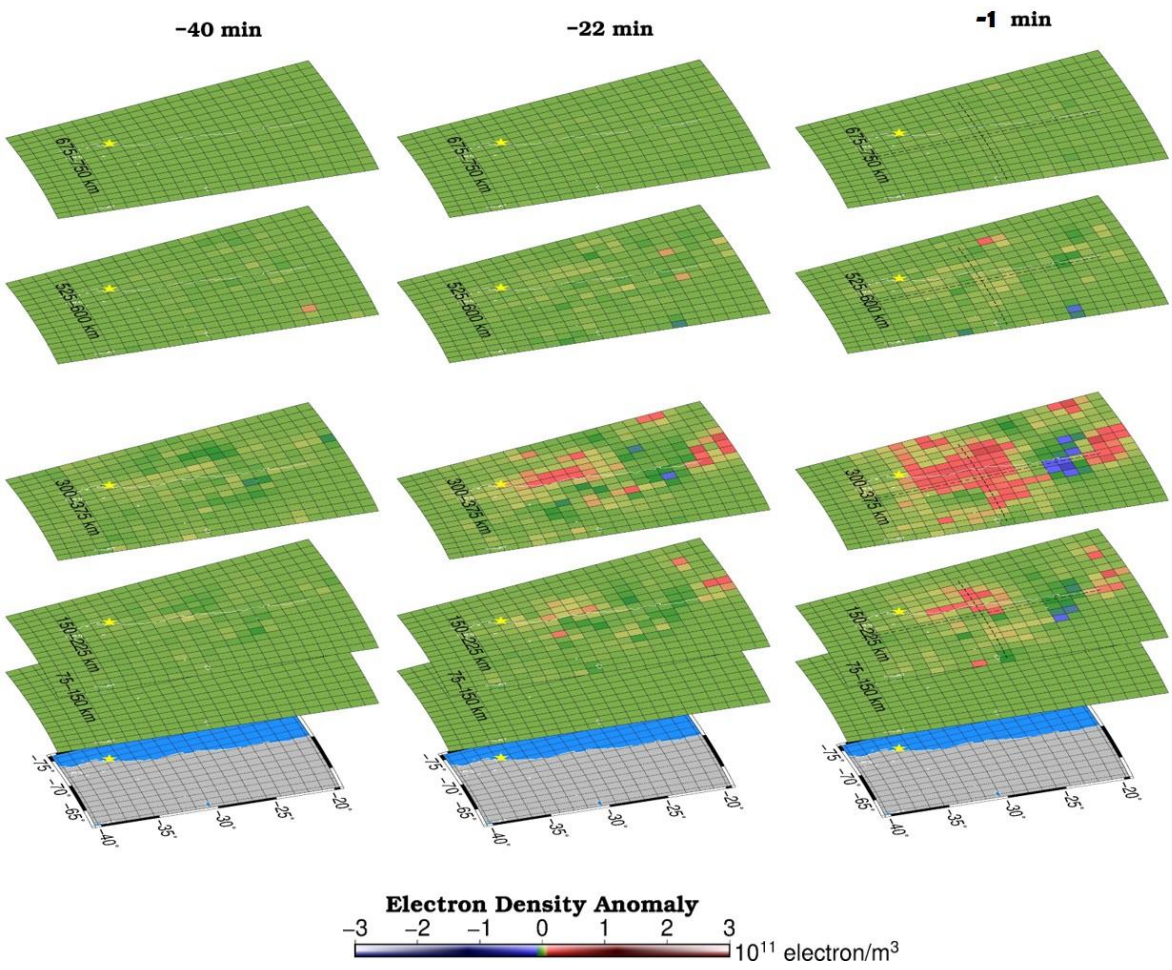


Figure 28. 3D tomography results of electron density anomalies 1 minute before the 2010 Maule earthquake (a). I also show the east-west (b) and north-south (c) profiles. Yellow stars show the latitude and longitude of the epicenter. White circles in (c) show selected positions used to draw Figure 31. The results for other epochs are given in Figure 29.



1122

1123

1124 **Figure 29**. 3D tomography results of electron density anomalies from 75-750 km altitudes at three
1125 epochs, 40, 22, and 1 minute before the 2010 Maule earthquake.

1126

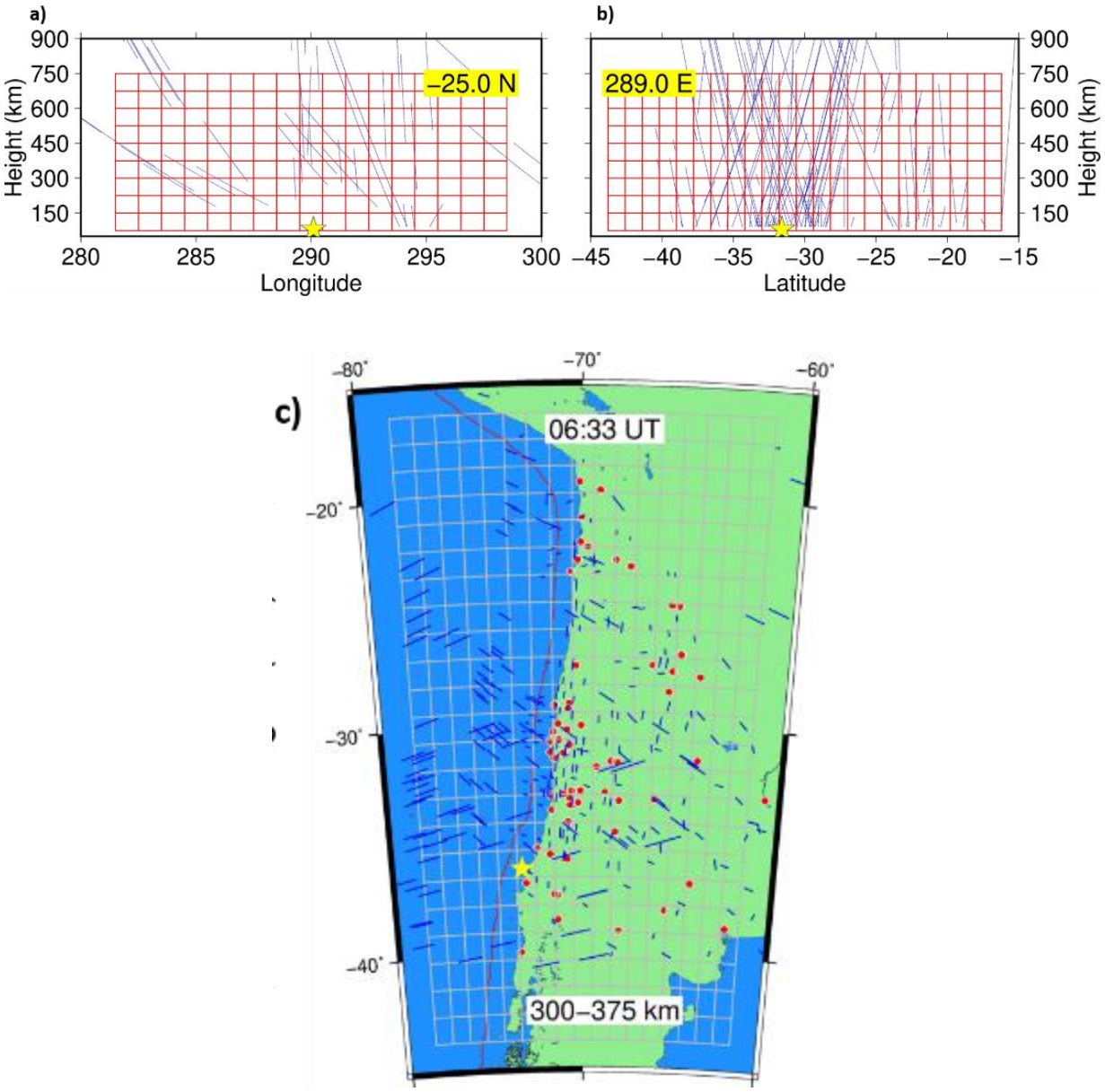


Figure 30. For vertical walls running east-west (a) and north-south (b) with the thickness of one block, the LoS penetrating those walls are plotted with blue lines. Blue short lines in the map (c) indicate the LoS of satellite-station pairs at the altitude 300-375 km (one layer of voxels) one minute before the earthquake. Sparseness of the data can be confirmed by comparing with Figures 10 and 15 for the 2011 Tohoku-oki case.

In Figure 31, I plot the average estimated positive electron density anomalies of the three different blocks at the altitudes of 300-375 km using 3D tomography result in Figure 28. This corresponds to Figure 22 in the 2011 Tohoku-oki case. I could see the smooth growth of the positive anomaly from 40 to 1 minutes, around 5.9-6.5 UT, before the mainshock. Unlike Figure 22, I did not include the growth curve for the negative anomalies. This is because the negative anomalies at high altitudes are hard to identify due to unfavorable distribution of the available LoS (Figure 30).

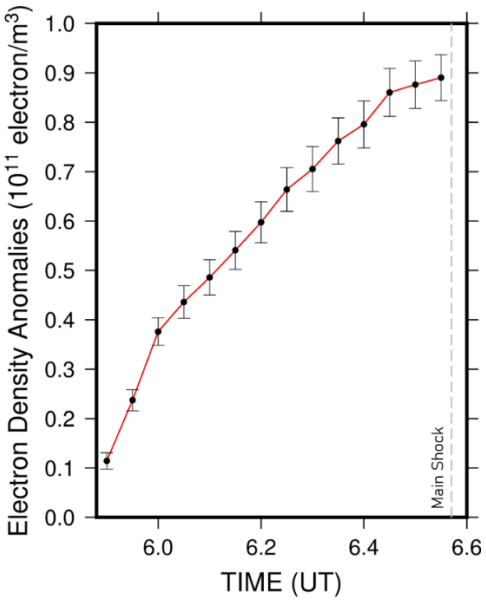
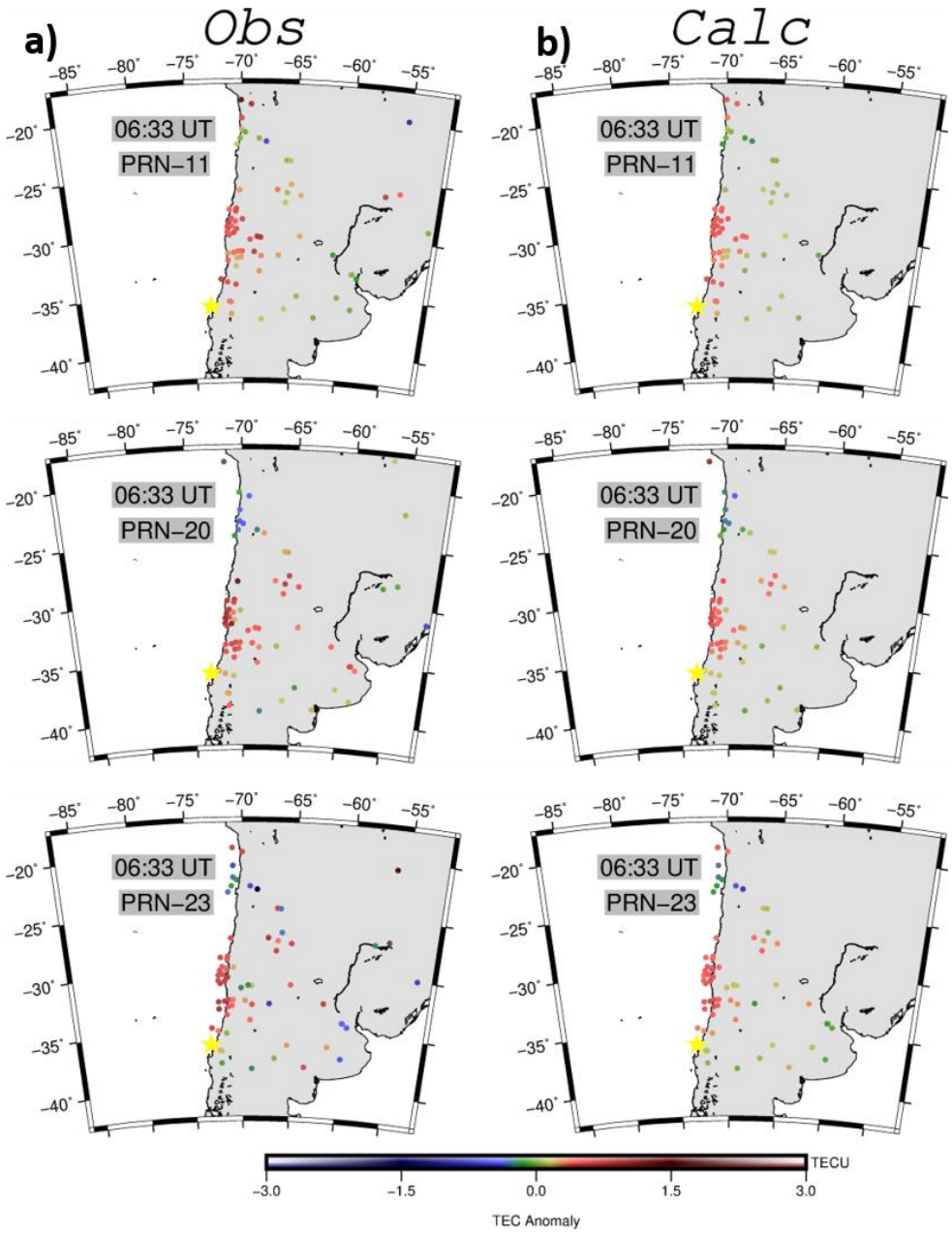


Figure 31. The growth of the average values of positive electron density anomalies at the three different blocks at the altitude of 300-375 km before the 2010 Maule earthquake. The error bars show the standard deviation around the average of the 7 voxels. The positions of the 7 voxels are indicated with white dots in Figure 28c.

Figure 32 compares the observed and calculated anomalies for four satellites, 11, 20, and 23 at the epoch 1 minute before the main shock. The "observed" anomalies (Figure 32a) are those obtained as the departure from the reference curves to VTEC time series, and I plotted them at

1151 their SIP. On the other hand, the “calculated” anomalies (Figure 32b) were derived as the sum of
1152 the products of the estimated electron density anomalies (Figure 28) and the penetration lengths of
1153 voxels along the LoS. Such calculated STEC anomalies are converted to VTEC for comparison
1154 with the observed anomalies. These two are expected to nearly coincide if the 3D tomography
1155 inversion is successful. We can see that the observed TEC anomalies are well reproduced by the
1156 estimated 3D electron density anomalies shown in Figure 28.



1157

1158 **Figure 32**. Comparison of the observed (a) and calculated (b) VTEC anomalies four 3 GPS
1159 satellites at the epoch at 06:33 UT, 1 minute before the earthquake. They are mostly consistent
1160 with each other demonstrating that the estimated 3D electron density anomaly structure well
1161 explains the observed TEC changes

4.6 Comparison with the 2011 Tohoku-oki and 2015 Illapel Earthquakes

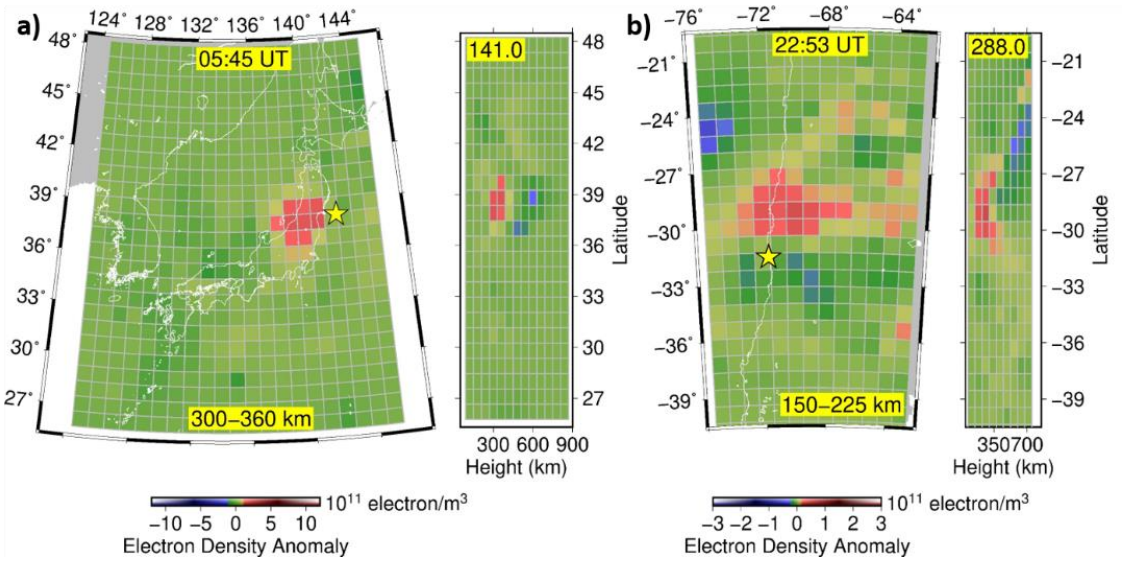
Now, there are three examples of the 3D distributions of ionospheric electron density anomalies immediately before large earthquakes, i.e. 2011 Tohoku-oki (M_w 9.0, this thesis), 2015 Illapel (M_w 8.3, He and Heki, 2018) and 2010 Maule earthquake (this thesis). They are compared in Figure 33. At a glance, we could see their similarities. They are composed of low-altitude positive anomalies and high-altitude negative anomalies. This does not apply for the 2010 Maule earthquake, but it is due to insufficient coverage of LoS in the region (Figure 27). Regarding the intensity of the anomaly, they largely differ (the two cases are drawn with different color palettes in Figure 33), i.e., the positive anomalies of the 2011 Tohoku-oki are ~7 times as strong as those of the 2015 earthquake. This would possibly reflect the difference in their magnitudes, M_w9.0 and 8.3, respectively.

The 2010 Maule earthquake has slightly stronger preseismic anomalies than the 2015 Illapel event (M_w8.3), although its magnitude (M_w8.8) is more similar to the 2011 Tohoku earthquake (M_w9.0). It might be because the background VTEC is low during the 2010 Maule earthquake, which occurred very early in the morning (03:34 AM in local time). Smaller amount of the original ionospheric electron density would result in smaller anomalies. Here I compare them using the ratios of the anomalies observed as GPS-TEC to the background values using three station-satellite pairs for each case. I found the ratio is $9.2 \pm 0.74\%$ for 2010 Maule Earthquake, $9.63 \pm 1.91\%$ for 2011 Tohoku Earthquake, and $6.0 \pm 0.61\%$ for 2015 Illapel Earthquake. These results suggest that the intensity of ionospheric anomalies depends on earthquake magnitudes. Such M_w dependences are also seen in the leading times and the intensities of the initial bending of the VTEC curves (Heki and Enomoto, 2015; He and Heki, 2017).

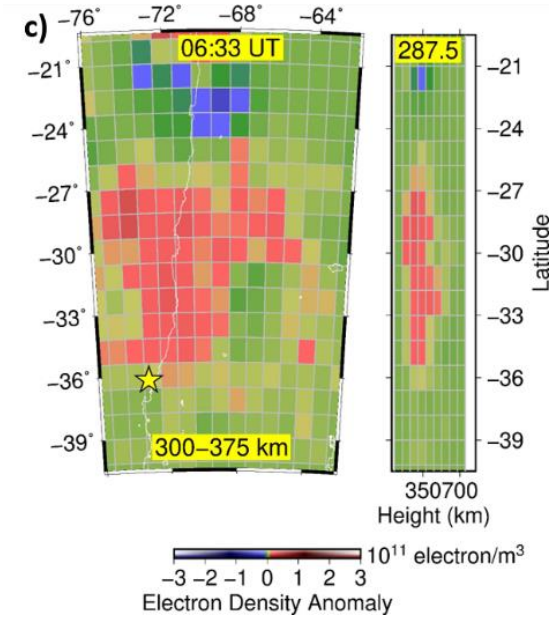
As for the altitude where the anomalies appeared, their vertical profiles suggest that the altitudes of the positive and negative anomalies before the 2011 earthquake (~300 and ~600 km) are somewhat higher than the 2015 earthquake (~200 and ~500 km). The altitude of the positive anomaly before the 2010 Maule earthquake is similar to that of the 2011 earthquake (~300 km). Hence, it seems that the 3D structure of the anomalies spatially expands for earthquakes with larger magnitudes.

On the other hand, horizontal extents of the anomalies before the 2011 and 2015 earthquakes are little different in the three cases, i.e. the positive anomalies lie within circles with diameter of ~300 km for 2011 Tohoku earthquake. The horizontal extent of the positive anomalies before 2010 Maule (M_w8.8) is much larger than the anomalies before 2015 Illapel (M_w8.3). The difference is almost twice in north-south and east-west dimensions (Figure 33b,c). It suggests that magnitudes control the size of the anomaly if other conditions are similar. As I discussed in the previous chapter, the strong positive anomalies of the 2011 Tohoku-oki earthquake did not occur directly above the epicenter but emerged above land. This suggests that the electron redistribution is due to electric fields made by surface electric charges. Such surface charges would be relatively stable on land, but they diffuse rapidly in the ocean due to high electric conductivity of sea water. Horizontal extent of the anomaly before the 2011 Tohoku-oki earthquake might have been limited by the land-sea distribution in the Japanese Islands, i.e. the anomaly may have expanded larger if NE Japan was a continental arc like Chile.

1203



1204



1205 **Figure 33**. The estimated 3D distributions of ionospheric electron density anomalies prior to the
1206 2011 Tohoku-oki earthquake (this thesis) (a), the 2015 Illapel earthquake (He and Heki, 2018) (b),
1207 and the 2010 Maule earthquake (this thesis) (c), drawn with the similar spatial scales. Each case is
1208 composed of two panels showing the plan view and the north-south profile at the longitude
1209 crossing the anomaly. (a) and (b,c) use different colour palettes, and the anomalies in (a) are ~7
1210 times as strong as in (b). The anomalies in (c) has larger horizontal extent than in (b) suggesting
1211 magnitude also controls the size of the anomaly if ambient land-ocean geometry is similar. The
1212 yellow stars are the epicenters of the three events.

Chapter 5: 3D Tomography of the Ionospheric Anomalies after Earthquakes: The 2011 Tohoku-oki Earthquake

The content of this chapter was published in Journal Geophysical Research Space Physics, Muafiry, I.N.and K. Heki, 3D tomography of the ionospheric anomalies immediately before and after the 2011 Tohoku-oki (M_w9.0) earthquake, J. Geophys. Res. Space Phys., 125, e2020JA027993, doi:10.1029/2020JA027993, 2020

5.1 Introduction: Tsunamigenic ionospheric anomalies

Ionospheric electron density drops (formation of the tsunami hole) are considered to occur right above the fault following the arrival of acoustic waves at the ionospheric F region ~10 minutes after the 2011 Tohoku-oki earthquake (Kakinami et al., 2012; Shinagawa et al., 2013; Zettergren and Snively, 2019). The physics related to this ionospheric hole is discussed in Chapter 5.6. Here I estimate the 3D structure of this postseismic anomaly to study its difference in structure and in position from the preseismic anomalies. This is expected to serve as a rebuttal to the opponents who claim that this hole served as a source of artifact for the preseismic TEC increases (Kamogawa and Kakinami, 2013; Masci et al., 2015).

5.2 Data set

GNSS data from the entire GEONET is used, 1,231 GNSS stations, to study the post-seismic anomalies of the 2011 Tohoku-oki earthquake. I used 8 GPS satellites (PRN 05, 09, 15, 18, 21, 26, 27, 28) visible from the studied region after the mainshock (05:46 UT). Unfortunately, GEONET did not track GNSS other than GPS in 2011. See also Chapter 2 for the detail of the input data. I did not use the GNSS data from Korea because of the remoteness of the Korean GNSS stations from the anomalies to the east of Honshu.

5.3 Data processing strategy

In Chapter 2.5, I explained two strategies to isolated TEC anomalies related to earthquakes. The first one is the modelling the temporal change of VTEC as a polynomial of time which is determined by least-squares method. The estimated models will serve as reference curves, and differences from these curves are defined as the anomalies. The other one is to make the difference

between medians of VTEC from two periods (before and after the start of the anomalies). Here I used the second strategy, i.e., I subtract the VTEC median before the ionospheric hole formation from VTEC after the hole formation to isolate the VTEC changes associated with the generation of the ionospheric hole.

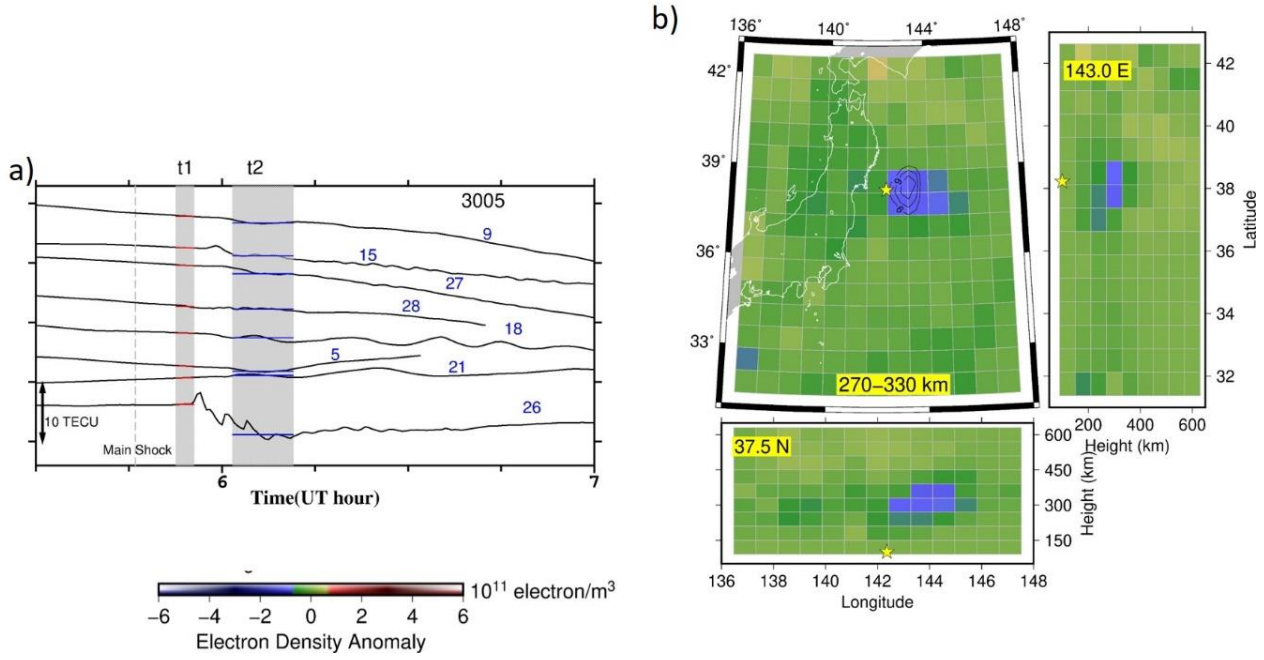


Figure 34. (a) VTEC time series of 8 GPS satellites, observed at 3005 in Kanto. The VTEC drops are defined as the difference between the median VTEC values in the two periods (grey rectangles). The flat red and blue lines within the two periods indicate the VTEC medians in the two periods, and I used their differences as the input to the 3D tomography. (b) 3D tomography of the electron depletion induced by the coseismic uplift and subsequent drop of the sea surface after the 2011 Tohoku-oki earthquake (yellow stars represent the epicenter). The contours in the plan view show the fault slips in the main shock (the contour interval is 3 meters). Spatially integrated amounts of negative and positive electron number changes are shown in Figure 22b in Chapter 3.

At first, I get the medians of VTEC from the two periods, i.e. 5:52-5:55 UT and 6:03- 6:11 UT (two grey rectangles in Figure 34a), in VTEC time-series of GNSS stations. These periods

correspond to times immediately before and after the ionospheric hole formation associated with the acoustic disturbance arrival. I do not use reference curves because the two periods are separated from each other by only ~10 minutes. The longer interval for the time window after the ionospheric hole formation was used because of the variety of acoustic disturbances occurring during this time window. In this method, we cannot remove the contribution from the long-term TEC decrease due to the increasing solar zenith angle. However, it would make a negative bias of the whole region and not as a localized anomaly.

I converted the difference of VTEC between the two epochs into STEC and used them as the input to our tomography program. I used the satellite positions at 6:00 UT, the time in the middle of the two periods. This would not cause a problem because LoS movements during the 10 minutes period is much less than the voxel size. I applied the same constraints as in the preseismic case to regularize the inversion.

5.4 Resolution tests

I performed the resolution test, by recovering patterns composed of a negative (-3.00×10^{11} el/m^3) anomaly in the F-region above the fault in neutral background (Figure 35a). The 3D tomography results (Figure 35b) well reproduced the assumed pattern of the negative anomaly. Again, the recovered amplitude was reduced to ~2/3 of the input model due to the constraints. In the map view, we see only weak smears in surrounding blocks not exceeding a few percent of the assumed anomaly. However, significant smears are seen in EW profile (lower panel of the output) because the resolution is poor in the direction of LoS connecting the land and the anomaly. The results of the two resolution tests show that our 3D tomography results are accurate enough in the

region of interest where the postseismic ionospheric hole appeared after the 2011 Tohoku-oki earthquake.

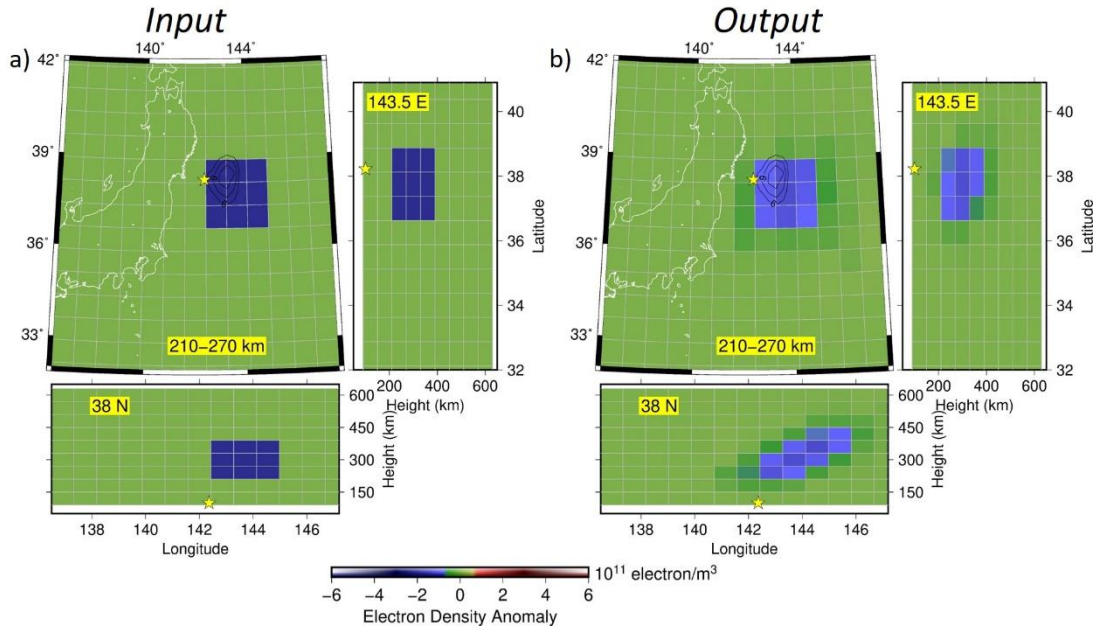


Figure 35. The resolution test for a compact negative anomaly off the Pacific coast of NE Japan. The upper, bottom, and right panels are horizontal view, latitudinal and longitudinal profiles of the anomalies of the assumed pattern (a) and the output of the 3D tomography with synthetic data (b).

5.5 Tomography result

Figure 34b shows the 3D structure of the recovered electron density anomalies associated with the formation of the postseismic ionospheric hole. The main part of the negative electron density anomaly lies at height of ~300 km above the tsunami source area (the area of large vertical crustal movements). An important point is that they occur offshore just above the area of large coseismic slips (contours in Figure 34b), which makes a clear contrast to the preseismic anomalies that occurred above land (Figure 17a, Chapter 3). Another important point is that the anomaly is composed only of the negative anomalies in contrast to the pair of positive and negative preseismic anomalies (Figure 17c Chapter 3). This suggests that the loss of electrons due to their recombination with positive ions is the main mechanism for the negative anomaly. Next, I will discuss the physical mechanism of the postseismic ionospheric hole based on these 3D tomography results.

5.6 Physical mechanism of post-seismic anomalies

The negative postseismic anomaly extends offshore beyond the large slip region as far as ~145E (Figure 34b). However, this is considered be due to the smearing as seen in the resolution test (Figure 35). An important point is that the post-seismic anomalies are mainly composed of negative changes. This makes a sharp contrast with the preseismic anomalies whose positive and negative changes are nearly balanced throughout their growth as shown in Figure 22b in Chapter 3.

These contrasts would reflect the different physical mechanisms responsible for the pre- and postseismic anomalies, i.e. the former is caused by electron transport, but the latter is caused

by the recombination of the electrons displaced downward by the acoustic disturbance as modelled by Kakinami et al. (2012) and Shinagawa et al. (2013). We also see that the dimension of the hole is consistent with the numerical simulation by Zettergren and Snively (2019).

5.7 Origin of variety of waveforms

In Chapters 3 and 5, I showed two different kinds of anomalies of the ionospheric electron density, the preseismic and the postseismic anomalies. Now I identified three electron density anomalies different in time and polarity, i.e. #1 the preseismic positive anomaly, #2 the preseismic negative anomaly, and #3 the postseismic negative anomaly. #1 and #2 start to grow simultaneously at low and high ionosphere ~40 minutes before the earthquake and decay after the earthquake, while #3 emerges shortly after the acoustic disturbance arriving 8-10 minutes after the earthquake and last for tens of minutes.

Heki (2011) noticed diversity of signatures of TEC disturbances related to earthquakes. For example, some LoS show only gradual growth and decay of positive signals (e.g. Sat.15- 3009 shown in Figure 11a) while other LoS show sudden decrease after the acoustic disturbances (e.g. Sat.26-0946 shown in Figure 11b). On the other hand, some LoS, like the cyan time series in Figure 11 top, show negative changes during the preseismic period. These varieties reflect the difference in the penetration of those LoS with the anomalies #1, #2, and #3. For example, Sat.15-3009 penetrated only #1, while Sat.26-0946 penetrated both #2 and #3.

Figure 36 explains the variety of waveforms of VTEC changes before and after the earthquake coming from the diversity in the penetrations of LoS with these three anomalies. There are four typical VTEC signatures observed in different satellite-station pairs, (1) LoS penetrating

both the preseismic positive and postseismic negative anomalies, (2) LoS without penetrating any anomalies, (3) LoS penetrating only preseismic positive, and (4) LoS penetrating only the postseismic negative anomalies. In Figure 36, I also show tomography profile before and after the earthquake and how the four LoS penetrate them. The VTEC time series are shown on top.

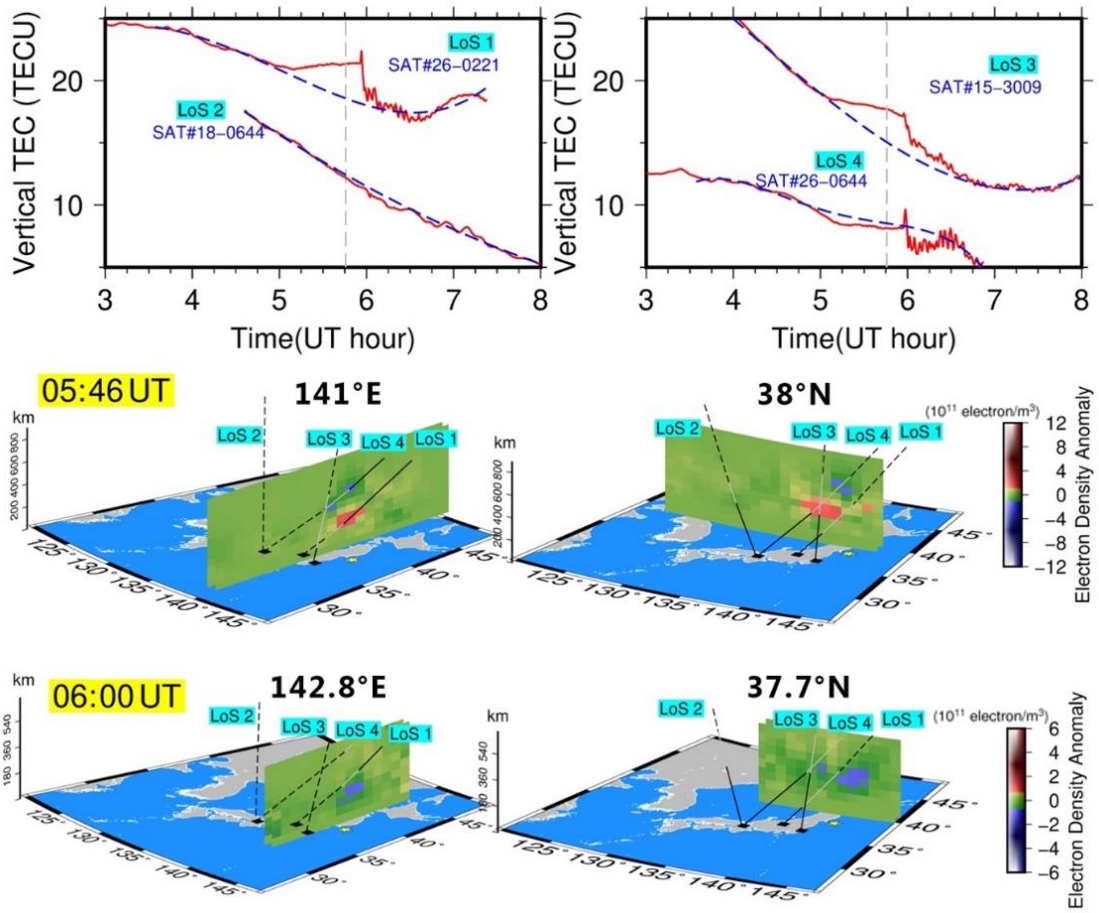


Figure 36. The 4 types of VTEC waveforms from different station-satellite pairs (upper panels), LoS 1 (Sa.26-0221) penetrating both the preseismic positive and postseismic negative anomalies, LoS 2 (Sat.18-0644) without penetrating any anomalies, LoS 3 (Sat.15-3009) penetrating only preseismic positive anomaly, and LoS 4 (Sat.26-0644) penetrating only the postseismic negative anomaly. Bottom panels are the 3D tomography result of preseismic and postseismic anomalies overlain with the LoS of the four examples. Black and grey lines indicate LoS in front of and within the profile (one block thick). Black dashed lines correspond to the LoS behind the profile.

Chapter 6: Conclusions and Recommendation

6.1 Conclusions

I studied the 3D structure of the ionospheric electron density anomalies immediately before the 2011 Tohoku-oki (M_w 9.0) and 2010 Maule (M_w 8.8) earthquakes by using GNSS-TEC data taken in Japan, South Korea, and South America in order to contribute to the understanding of the physical processes responsible for the preseismic ionospheric anomalies found by Heki (2011).

I paid special attention to the detail of the method to obtain the TEC anomalies as the input to the 3D tomographic inversion program. I optimized the polynomial degrees for the reference curves using the L-curve method. The exclusion windows were set up to estimate the reference curves without being influenced by ionospheric disturbances due to earthquakes. The start of the window was defined by the positive bending of the TEC time series detected by statistical techniques in an earlier study (Heki and Enomoto, 2015). The end of the window was selected carefully to avoid the interference from the postseismic ionospheric hole.

The linear inversion is stabilized by continuity and altitude-dependent constraints, and the performance of the method was confirmed by trying 3D tomography to artificial patterns, a classical checkerboard pattern and a realistic pattern of a pair of positive and negative anomalies. The tests showed that I can resolve electron density anomalies in the ionosphere above regions with enough number of ground stations. However, it is not expected that we can identify the upper negative anomaly before the 2010 Maule earthquake.

The 3D tomography results of the two cases, together with another study for the 2015 Illapel earthquake (He and Heki, 2018), showed that the preseismic ionospheric anomaly has

following similarities; (1) They are composed of pairs of low-altitude positive and high-altitude negative (not detected for the 2010 Maule earthquake due to limited LoS distribution) electron density anomalies. (2) They occur above the land area close to the submarine faults. (3) They have clear onsets a few tens of minutes before earthquakes (~40 min before 2011 Tohoku-oki, and Maule, and ~20 minutes before the Illapel earthquakes) and grow with decaying rates.

I compared strengths of the electron density anomalies before these three earthquakes. For example, the positive electron density anomalies before the 2011 Tohoku-oki case was seven times as strong as that for the 2015 Illapel case. The strength of the preseismic anomalies was also found to be controlled by the background electron density on the earthquake days. For example, the positive electron density anomaly before the 2010 Maule earthquake was only as strong as in the 2015 Illapel case. This might be due to smaller electron density in the 2010 earthquake that occurred after the midnight.

I also compared the dimensions of the electron density anomalies before these three earthquakes. The 2011 earthquake showed positive anomalies lying above the land, and not above the submarine epicenter. On the other hand, the 2010 Maule and 2015 Illapel earthquakes showed positive anomalies located above the coast (i.e. both above land and above ocean close to the coast). This means that the anomaly partly smears out to the ocean, but it is difficult to tell if it comes from inadequate density and distribution of the ground GNSS stations. The areal extent of the anomaly before the 2015 case was similar to the 2011 case. This would be due to the different situation of land-ocean distribution for the two cases, e.g., the land area is limited in NE Japan, an island arc, in the 2011 Tohoku-oki case. The 2010 Maule earthquake showed the largest horizontal extent. This might reflect a larger proportion of land in a continental arc like Chile.

I presented the model for the physical process of the preseismic ionospheric anomalies consistent with such 3D structure proposed in Muafiry and Heki (2020). Micro-scale cracks and dislocations could mobilize positive electric charges shortly before large earthquakes. They would concentrate near the land surface and generate upward electric fields. The field would then reach the ionosphere and generates electromotive forces to make electrons move down along the geomagnetic fields. This would continue until the induced downward electric field cancels the upward fields due to crustal electric charges, making the electric potential uniform along the magnetic field.

The current will depend on the along-B component of the external electric field and the density of free electrons as a function of altitude. The nonuniform electric currents would result in convergence/divergence of electrons and make positive/negative electron density anomalies at the lower/higher ionosphere along the magnetic field, the structure consistent with those found for these three earthquakes by 3D tomography. This upward current (downward electron migration) would also make eastward/westward magnetic field in regions to the south/north of the epicenter before earthquakes in northern/southern hemisphere.

I also studied the 3D structure of the postseismic anomalies of 2011 Tohoku-oki earthquake and found that the negative electron density anomaly emerged offshore just above the submarine fault. Variety of TEC change patterns observed before and after the 2011 Tohoku-oki earthquake is understood by different combinations of the penetrations of LoS with such electron density anomalies.

6.2 Recommendation

1. There are variety of features of scientific importance in the ionosphere. Conventional sensors, such as satellite in-situ observations and ionosondes, used to require a lot of efforts and resources to observe ionosphere. Recent launch of GNSS satellite and deployment of ground networks of continuous GNSS receivers made such studies much easier for everyone to start. Such ionospheric studies using GNSS data are especially suitable for university laboratories with limited human and financial resources.

2. In comparison with the analysis of total electron content (TEC) along line-of-sights (LoS), 3D tomography provides a robust way to study the 3D structure of various ionospheric disturbances. The targets of 3D tomography are not limited to those related to surface phenomena such as earthquakes. It can be applied for various space weather phenomena including various traveling ionospheric disturbances and sporadic-E irregularities. 3D tomography technique gives opportunity for human to understand the earth's upper atmosphere better.

3. Ionospheric anomalies occurring immediately before large earthquake, found by Heki (2011), can become a key phenomenon toward practical earthquake prediction and mitigation of earthquake disasters in the future. 3D tomography for the electron density anomalies for such phenomena provides important insight into the physical processes responsible for them. Based on the 3D structure of the preseismic ionospheric anomalies, I proposed one such model assuming that surface electric charge redistribute ionospheric electrons through electric fields. In the future, detailed observations of the ground electric charges might give a conclusive evidence for the validity of such models.

4. Regarding the practical aspect, sophisticated statistical techniques would be necessary to detect preseismic ionospheric anomalies as discussed in this thesis, together with automated real-time analyses of GNSS-TEC data to establish operational early warning system of large earthquakes.

References

Astafyeva, E. and K. Heki (2009), Dependence of waveform of near-field coseismic ionospheric disturbances on focal mechanisms, *Earth Planet. Space*, *61*, 939-943.

Astafyeva, E., K. Heki, V. Kiryushkin, E. Afraimovich, S. Shalimov (2009), Two-mode long-distance propagation of coseismic ionosphere disturbances, J. Geophys. Res., 114, A10307, doi:10.1029/2008JA013853.

Astafyeva, E., P. Lognonné, and L. Rolland (2011), First ionospheric images of the seismic fault slip on the example of the Tohoku-oki earthquake, *Geophys. Res. Lett.*, *3*8, L22104. doi:10.1029/2011GL049623

Astafyeva, E. and K. Shults (2019), Ionospheric GNSS imagery of seismic source: Possibilities, difficulties, and challenges, *J. Geophys. Res. Space Phys.*, *124*, 534-543. doi:10.1029/2018JA026107.

Austen JR, Franke J, Liu CH (1988) Ionospheric imaging using computerized tomography. *Radio Sci., 23:299–307*, doi:10.1029/RS023i003p00299

Cahyadi, M. N., and K. Heki (2015), Coseismic ionospheric disturbance of the large strike-slip earthquakes in North Sumatra in 2012: M_w dependence of the disturbance amplitudes, *Geophys. J. Int., 200(1*), 116-129, doi:10.1093/gji/ggu343.

Calais, E. and J. B. Minster (1995), GPS detection of ionospheric perturbations following the January 17, 1994, Northridge earthquake, *Geophys. Res. Lett.*, *22*, 1045–1048, doi:10.1029/95GL00168.

1450 Chen, C. H. A. Saito, C. H. Lin, M. Yamamoto, S. Suzuki, G. K. Seemala (2016), Medium-scale
1451 traveling ionospheric disturbances by three-dimensional ionospheric GPS tomography, *Earth,*
1452 *Planets and Space, 68:32, DOI 10.1186/s40623-016-0412-6*

1453 Choi, B.-K., and J. Hong (2019), Observation of the fast-traveling ionospheric disturbances
1454 induced by the 2017 North Korean missile, Adv. Space Res., 63, 2598-2608,
1455 doi:10.1016/j.asr.2018.12.033.

1456 Coster, A., J. Williams, A. Weatherwax, W. Rideout, and D. Herne (2013), Accuracy of GPS total
1457 electron content: GPS receiver bias temperature dependence. *Radio Science, 48,* 190–196.
1458 doi:10.1002/rds.20011

1459 Freund, F. T. (2011), Pre-earthquake signals: Underlying physical processes. *Journal Asian Earth*
1460 *Sci.,41(4-5),* 383–400. doi:10.1016/j.jseaes.2010.03.00 9

1461 Freund, F. (2013), Earthquake forewarning - A multidisciplinary challenge from the ground up to
1462 space, *Acta Geophys., 6(14),* 775-807, doi:10.2478/s11600-013-0130-4.

1463 Garcia, R., F. Crespon, V. Ducic, P. Lognonné (2005), Three-dimensional ionospheric tomography
1464 of post-seismic perturbations produced by the Denali earthquake from GPS data, *Geophys. J.*
1465 *Int., 163, 1049–106,* doi: 10.1111/j.1365-246X.2005.02775.x

1466 He, L., and Heki, K. (2016). Three-dimensional distribution of ionospheric anomalies prior to three
1467 large earthquakes in Chile. *Geophys. Res. Lett., 43,* 7287–7293. doi:10.1002/2016GL069863

1468 He, L., and K. Heki (2017), Ionospheric anomalies immediately before M_w7.0–8.0 earthquakes. *J.*
1469 *Geophys. Res. Space Phys.*, 122, 8659–8678. doi:10.1002/2017JA024012

He, L., and K. Heki (2018), Three-dimensional tomography of ionospheric anomalies immediately before the 2015 Illapel earthquake, Central Chile, *J. Geophys. Res. Space Phys.*, 123, 4015–4025. doi:10.1029/2017JA024871

He, L., K. Heki, and L. Wu (2018), Three-dimensional and trans-hemispheric ionospheric electron density changes by the great Solar eclipse in North America on 21 August 2017, *Geophys. Res. Lett.*., 45, 10,933-10,940, doi:10.1029/2018GL080365.

Heki, K. and J.-S. Ping (2005), Directivity and apparent velocity of the coseismic ionospheric disturbances observed with a dense GPS array, *Earth Planet. Sci. Lett.*, *236*, 845–855, doi:10.1016/j.epsl.2005.06.010.

Heki, K. (2006), Explosion energy of the 2004 eruption of the Asama Volcano, Central Japan, inferred from ionospheric disturbances, *Geophys. Res. Lett.*, *33*, L14303, doi:10.1029/2006GL026249

Heki, K. (2011), Ionospheric electron enhancement preceding the 2011 Tohoku-oki earthquake. *Geophys. Res. Lett.*, 38, L17312. doi:10.1029/2011GL047908

Heki, K. and Y. Enomoto (2013), Preseismic ionospheric electron enhancements revisited, *J. Geophys. Res.*, *118*, 6618-6626, doi:10.1002/jgra.50578.

Heki, K. and Y. Enomoto (2014), Reply to comment by K. Heki and Y. Enomoto on "Preseismic ionospheric electron enhancements revisited", *J. Geophys. Res. Space Phys.*, *119*, doi:10.1002/2014JA020223.

1489 Heki, K., and Y. Enomoto (2015), M_w dependence of the preseismic ionospheric electron
1490 enhancements. *J. Geophys. Res. Space Phys.*, *120*, 7006–7020, doi:10.1002/2015JA021353.

1491 Heki, K. (2021), Chapter 5-3: Ionospheric disturbances related to earthquakes in *Advances in*
1492 *ionospheric research: Current understanding and challenges*, Wiley/AGU Book Space Physics
1493 and Aeronomy, Volume 3, edited by C. Huang and G. Lu, pp.320, ISBN:978-1-119-50755-0.

1494 Iwata, T. and K. Umeno (2016), Correlation Analysis forpreseismic Total Electron Content
1495 Anomalies around the 2011 Tohoku-oki Earthquake, *J. Geophys. Res. Space Phys.*, *121*, 8969-
1496 8984, doi:10.1002/2016JA023036

1497 Jara-Munoz, J., D. Melnick, D. Brill, M. R. Strecker (2015), Segmentation of the 2010 Maule
1498 Chile earthquake rupture from a joint analysis of uplifted marine terraces and seismic-cycle
1499 deformation patterns, Quaternary Science Reviews, 113:171-192,
1500 doi:10.1016/j.quascirev.2015.01.005

1501 Kakinami, Y., M. Kamogawa, Y. Tanioka, S. Watanabe, A. R. Gusman, J.-Y. Liu, Y. Watanabe,
1502 and T. Mogi (2012), Tsunamigenic ionospheric hole, *Geophys. Res. Lett.*, *39*, L00G27,
1503 doi:10.1029/2011GL050159

1504 Kamogawa, M., and Y. Kakinami (2013), Is an ionospheric electron enhancement preceding the
1505 2011 Tohoku-oki earthquake a precursor? *J. Geophys. Res. Space Phys.*, *118*, 1751–1754,
1506 doi:10.1002/jgra.50118.

1507 Kelley, M.C. (2009), The Earth’s Ionosphere: Plasma Physics and Electrodynamics, Elsevier, 2nd
1508 ed.

Kelley, M. C., W. E. Swartz, and K. Heki (2017), Apparent ionospheric total electron content variations prior to major earthquakes due to electric fields created by tectonic stresses, *J. Geophys. Res. Space Phys., 122*, doi:10.1002/2016JA023601.

Kundu, B., B. Senapati, A. Matsushita,and K. Heki (2021), Atmospheric wave energy of the 2020 August 4 explosion in Beirut, Lebanon, from ionospheric disturbances, *Sci. Rep.,11*, 2793, doi:10.1038/s41598-021-82355-5.

Kuo, C. L., L. C. Lee, and J. D. Huba (2014), An improved coupling model for the lithosphere-atmosphere-ionosphere system, *J. Geophys. Res. Space Phys., 119*, 3189-3205, doi:10.1002/2013JA019392.

Kwon, J. (2012), Korea Geodetic Framework for Sustainable Development, Nineteenth United Nations Regional Cartographic, Conference for Asia and the Pacific, E/CONF.102/IP.17.

Le, H., Liu, J. Y., and Liu, L. (2011), A statistical analysis of ion- ospheric anomalies before 736 M6.0+ earthquakes during 2002–2010. *Journal of Geophysical Research, 116*, A02303. doi:10.1029/2010JA015781

Li, M., and Parrot, M. (2013), Statistical analysis of an iono- spheric parameter as a base for earthquake prediction. *Journal of Geophysical Research, 118, 3731–3739.* doi:10.1002/ jgra.50313

Liu, J.-Y., Y.-B. Tsai, K.-F. Ma, Y.-I. Chen, H.-F.Tsai, C.-H. Lin, M. Kamogawa, C.-P. Lee, (2006), Ionospheric GPS total electron content (TEC) disturbances triggered by the 26 December

2004 Indian Ocean tsunami. *Journal of Geophysical Research, 111, A05303,* doi:10.1029/2005JA011200

Liu, J. Y., Chen, Y. I., Chuo, Y. J., and Tsai, H. F. (2001), Variations of ionospheric total electron content during the Chi-Chi earthquake. *Geophysical Research Letters, 28,* 1383–1386.

Masci, F., J. Thomas, F. Villani, J. Secan, and N. Rivera (2015), On the onset of ionospheric precursors 40 min before strong earthquakes, *J. Geophys. Res. Space Phys., 120(2),* 1383-1393, doi:10.1002/2014JA020822.

Muafiry, I. N. and K. Heki (2020), 3D tomography of the ionospheric anomalies immediately before and after the 2011 Tohoku-oki (Mw9.0) earthquake, *J. Geophys. Res. Space Phys., 125,* e2020JA027993, doi:10.1029/2020JA027993.

Muafiry, I. N., K. Heki, and J. Maeda (2018), 3D tomography of midlatitude sporadic-E in Japan from GNSS-TEC data. *Earth, Planets Space,70(1*). doi:10.1186/s40623-018-0815-7

Němec, F., Santolik, O., Parrot, M., and Berthelier, J. J. (2008), Spacecraft observations of electromagnetic perturbations connected with seismic activity. *Geophysical Research Letters, 35*, L05109. doi:10.1029/2007GL032517

Occhipinti, G., P. Lognonné, E. A. Kherani, and H. Hébert (2006), Three-dimensional waveform modeling of ionospheric signature induced by the 2004 Sumatra tsunami, *Geophys. Res. Lett., 33, L20104*, doi:10.1029/2006GL026865.

Otsuka Y, Kotake N, Shiokawa K, Ogawa T, Tsugawa T, Saito A (2011), Statistical study of medium-scale traveling ionospheric disturbances observed with a GPS receiver network in Japan.

In: *Aeronomy of the earth's atmosphere and ionosphere, IAGA Special Sopron Book Series, vol 2, part 3*, pp 291–299. doi:10.1007/978-94-007-0326-1_21

Ozawa, S., T. Nishimura, H. Suito, T. Kobayashi, M. Tobita, and T. Imakiire (2011), Coseismic and postseismic slip of the 2011 magnitude-9 Tohoku-Oki earthquake. *Nature, 475*, 373-376. doi:10.1038/nature10227

Rideout, W., and A. Coster (2006), Automated GPS processing for global total electron content data, *GPS Solut., 10*, 219–228, doi:10.1007/s10291-006-0029-5.

Rolland, L. M., G. Occhipinti, P. Lognonné, A. Loevenbruck (2010), Ionospheric gravity waves detected offshore Hawaii after tsunamis, *Geophys. Res. Lett.*, vol. 37, L17101, doi:10.1029/2010GL044479.

Rolland, L. M., M. Vergnolle, J.-M. Nocquet, A. Sladen, J.-X. Dessa, F. Tavakoli, H. R. Nankali, and F. Cappa (2013), Discriminating the tectonic and non-tectonic contributions in the ionospheric signature of the 2011, M_w7.1, dip-slip Van earthquake, Eastern Turkey, *Geophys. Res. Lett., 40*, 2518–2522, doi:10.1002/grl.50544.

Saito S, S. Suzuki, M. Yamamoto, C.H. Chen, A. Saito (2016), Real-time Ionosphere Monitoring by Three-dimensional Tomography Over Japan. *In: Proc. 29th int. tech. meeting, Satellite Division of the Institute of Navigation (ION GNSS+2016), Portland, Oregon. pp 706–713*

Sakai, T. (2005), Bias error calibrations for observing ionosphere by GPS network, *IEICE Trans. Comm., J88-B*, 2382-2389. (in Japanese)

Seemala G. K., M. Yamamoto, A. Saito, C. H. Chen (2014), Three-dimensional GPS ionospheric tomography over Japan using constrained least squares. J. *Geophys Res Space Phys 119:3044–3052*. https://doi. org/10.1002/2013JA019582

Shinagawa, H., T. Tsugawa, M. Matsumura, T. Iyemori, A. Saito, T. Maruyama, H. Jin, M. Nishioka, and Y. Otsuka (2013), Two-dimensional simulation of ionospheric variations in the vicinity of the epicenter of the Tohoku-oki earthquake on 11 March 2011, *Geophys. Res. Lett., 40*, 5009-5013, doi:10.1002/2013GL05762

Song, R., K. Hattori, X. Zhang, S. Sanaka (2020), Seismic-ionospheric effects prior to four earthquakes in Indonesia detected by the China seismo-electromagnetic satellite, *Journal of Atmospheric and Solar-Terrestrial Physics 205, 105291,* https://doi.org/10.1016/j.jastp.2020.105291

Tang, J., Y. Yao, L. Zhang, J. Kong (2015), Tomographic reconstruction of ionospheric electron density during the storm of 5-6 August 2011 using multi-source data, *Sci. Rep. 5, 13042*, doi: 10.1038/ srep13042

Thomas, J.N., Huard, J., and Masci, F. (2017). A statistical study of global ionospheric map total electron content changes prior to occurrences of M≥6.0 earthquakes during 2000–2014. *Journal of Geophysical Research, 122*, 2151–2161. doi:10.1002/2016JA023652

Tsuji, H., and Hatanaka, Y. (2018). GEONET as Infrastructure for Disaster Mitigation. *J. Disaster Res., 13(3),* 424-432.

1586 Utada, H., and H. Shimizu (2014), Comment on “Preseismic ionospheric electron enhancements
1587 revisited” by K. Heki and Y. Enomoto, *J. Geophys. Res. Space Phys., 119(7)*, 6011-6015,
1588 doi:10.1002/2014JA020044.

1589 Zettergren, M. D. and J. B. Snively (2019), Latitude and longitude dependence of ionospheric TEC
1590 and magnetic perturbations from infrasonic-acoustic waves generated by strong seismic events,
1591 *Geophys. Res. Lett., 46*, 1132–1140, doi:10.1029/2018GL081569.

1592